ACS Biomaterials SCIENCE & ENGINEERING

pubs.acs.org/journal/abseba

Article

3D Printed Microneedles for the Transdermal Delivery of NAD$^+$ Precursor: Toward Personalization of Skin Delivery

Masood Ali, Sarika Namjoshi, Khanh Phan, Xiaoxin Wu, Indira Prasadam, Heather A. E. Benson, Tushar Kumeria,* and Yousuf Mohammed*

Cite This: https://doi.org/10.1021/acsbiomaterials.4c00905

Read Online

ACCESS | Metrics & More | Article Recommendations | Supporting Information

ABSTRACT: 3D printing of microneedles (μNDs) for transdermal therapy has the potential to enable patient personalization based on the target disease, site of application, and dosage requirements. To convert this concept to reality, it is necessary that the 3D printing technology can deliver high resolution, an affordable cost, and large print volumes. With the introduction of benchtop 4K and 8K 3D printers, it is now possible to manufacture medical devices like μNDs at sufficient resolution and low cost. In this research, we systematically optimized the 3D printing design parameters such as resin viscosity, print angle, layer height, and curing time to generate customizable μNDs. We have also developed an innovative 3D coating microtank device to optimize the coating method. We have applied this to the development of novel μNDs to deliver an established NAD$^+$ precursor molecule, nicotinamide mononucleotide (NMN). A methacrylate-based polymer photoresin (eSun resin) was diluted with methanol to adjust the resin viscosity. The 3D print layer height of 25 μm yielded a smooth surface, thus reducing edge-ridge mismatches. Printing μNDs at 90° to the print platform yielded 84.28 ± 2.158% (n = 5) of the input height thus increasing the tip sharpness (48.52 ± 10.43 μm, n = 5). The formulation containing fluorescein (model molecule), sucrose (viscosity modifier), and Tween-20 (surface tension modifier) was coated on the μNDs using the custom designed microtank setup, and the amount deposited was determined fluorescently. The dye-coated μND arrays inserted into human skin (*in vitro*) showed a fluorescence signal at a depth of 150 μm (n = 3) into the skin. After optimization of the 3D printing parameters and coating protocol using fluorescein, NMN was coated onto the μNDs, and its diffusion was assessed in full-thickness human skin *in vitro* using a Franz diffusion setup. Approximately 189 ± 34.5 μg (5× dipped coated μNDs) of NMN permeated through the skin and 41.2 ± 7.53 μg was left in the skin after 24 h. Multiphoton microscopy imaging of NMN-coated μND treated mouse ear skin *ex vivo* demonstrated significantly (p < 0.05) increased free-unbound NADPH and reduced fluorescence lifetime of NADPH, both of which are indicative of cellular metabolic rates. Our study demonstrates that low-cost benchtop 3D printers can be used to print high-fidelity μNDs with the ability to rapidly coat and release NMN which consequently caused changes in intracellular NAD$^+$ levels.

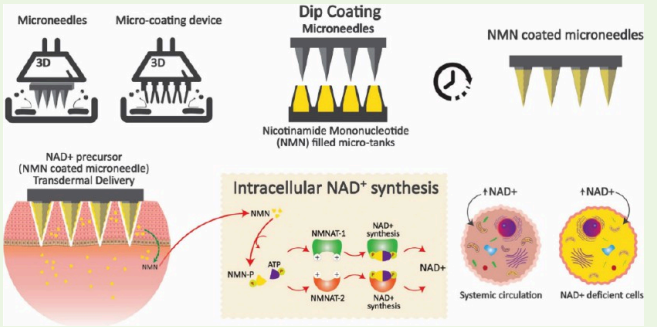

KEYWORDS: *microneedle, 3D printing, NAD+ precursor, nicotinamide mononucleotide, thin film coating, transdermal drug delivery, multiphoton imaging, personalized delivery*

1. INTRODUCTION

There are various important design criteria to consider when designing and fabricating 3D-printed microneedles (μNDs). Of all the design criteria, μND height is considered to be the most important factor, since the sub-micrometer height range of the μND allows for seamless insertion with minimal pain[1−4] and determines the depth at which the drug is delivered into the skin.[5] Another important design factor is the aspect ratio, i.e., the needle height/base diameter ratio. The aspect ratio of the μND influences both the ease of insertion[6] and the structural mechanical integrity.[7,8] While higher aspect ratio μNDs are easier to insert,[7,8] a lower aspect ratio results in mechanically stronger needles.[9] The μND tip diameter is also a key design factor ensuring efficient μND skin insertion.[10] To achieve efficient μND skin insertion without causing any pain sensation, the ideal μND structural dimensions have been reported to be as follows: μND shaft height: 500−800 μm,[11−13] μND base width: 150−300 μm.[14−18] Therefore, the control of these dimensional parameters of μNDs is important, as this allows for tailoring of the μND utility.

Received: May 16, 2024
Revised: September 12, 2024
Accepted: September 12, 2024

Microelectromechanical systems (MEMS) fabrication techniques, which includes drawing lithography,[19,20] electrical discharge machining,[21] direct laser micromachining,[22] and micromilling,[23] are generally employed in the fabrication of μND arrays. Although these techniques can yield μNDs with excellent microtopographical features, they either utilize expensive specialized instruments and/or require advanced manufacturing facilities such as clean rooms. Therefore, researchers commonly utilize μND molds from engineering workshops. Replica molds offer the advantage of low cost, repeatability, scalability, and reusability with a wide range of thermoplastic, thermoset, and swellable/hydrogel-type polymers. However, where μND dimensional parameters such as the aspect ratio, array size, and interneedle distance need to be tailored to a patient's needs, fabricating molds with high dimensional accuracy would be both expensive (use of laser drilling method) and time-prohibitive (lengthy turn-around times). Extrusion-based subtractive 3D printing is an alternative where low-cost μND molds can be fabricated from master μNDs that allow for freedom of design parameters, however, these methods require multiple manual steps and are labor intensive,[24−26] often suffering from interlayer distortion[27] and poor surface quality.[28] Therefore, an additional step is introduced to overcome the resolution limitation, that involves dry or wet etching of the 3D model to make sharper μNDs.[29,30] To overcome this two-step fabrication technique while maintaining better resolution in printing sharper μNDs, vat photopolymerization-based additive manufacturing (AM) 3D printing has been extensively explored including highly sensitive yet expensive two-photon polymerization[31,32] and continuous liquid interface production,[5,33] in which a liquid photosensitive polymer vat is selectively cured/solidified using light. However, most research conducted so far to improve print resolution has been on expensive 3D printers; although yielding high 3D model input to output ratio, they are not convenient for on-demand rapid prototyping of μND manufacturing.[34−42] On the other hand, low-cost stereolithography (SLA) and digital light processing (DLP) based desktop 3D printers only managed to fabricate μNDs that exhibited some but not all of the three key geometric parameters required for high-quality μNDs consisting of good tip sharpness, sub-micrometer height, and high-aspect ratio, which are also connected to 3D model input to output ratio.[38,43−47] In this study, we present a simple and customizable 3D printed μND fabrication technique by optimizing 3D printing design parameters such as modifying resin, print angle, and print aspect ratio. In doing so, we aim to address the issues and limitations associated with previous μND fabrication through low-cost desktop 3D printers (Figure S1), often suffering from large tip diameter,[48,49] low output height,[34,50−53] and/or low aspect ratios,[34,51−53] by demonstrating the fabrication of highly accurate and resolved μND structures. We show that by reducing the viscosity of the resin vat, increased intensity of light waves can penetrate through the resin, thus improving the 3D model input to output ratio. To further improve the input to output ratio and μND tip radii, the 3D print angle was optimized to 90°, which increased the input to output ratio to 87%, a vast improvement compared to past studies.[35,36,54−61]

The other challenge of delivering a drug through solid μNDs is the coating of a drug on the surface of the μND itself. Researchers in the past employed dip coating techniques[62−67] to improve the accuracy and uniformity of coating, but these produced variable results. Surface tension of the coating solution leads to nonuniform coating throughout the array, subsequently causing drug loss and bluntness of the needle tip. Prasunitz et al.[63] and Liang et al.[66,67] demonstrated that by enhancing coating formulation attributes (addition of surfactants and viscosity enhancers thus reducing surface tension and improving wetting) and by increasing the dipping time, uniform coating on the μND surface can be achieved with minimal drug loss. However, the thermodynamics of the coating solution in miniaturized coating tanks acts differently. This is due to increased surface tension of the coating solution around the edges of the miniaturized coating tank, consequently forming concave menisci where the height of the coating solution on the edges of the coating tank is higher compared to the coating solution away from the edges.[68] To alleviate this issue, we propose and present a detailed investigation of an on-demand 3D printed microtank fabrication that has the ability to uniformly coat individual μNDs in the array with controlled wetting. This was achieved by 3D printing individual microtanks on a solid base, where the diameter of the microtank opening is smaller than the diameter of the μND base, such that when the μNDs were dipped into the tank, the larger diameter of the μND base would stop the complete immersion of the μND shaft. We also demonstrate that by increasing the dipping frequency of μNDs in the microtanks, approximately 300 μg of an established NAD^+ precursor molecule, nicotinamide mononucleotide (NMN), was uniformly coated on the shafts of the μNDs only. Successful insertion of NMN coated μNDs was achieved in full thickness human skin, with approximately 200 μg of NMN diffused from the μNDs and permeated through the skin.

NMN has been implicated in age associated cellular regeneration processes such as protection against proinflammatory-mediated impairment of pancreatic islet cells,[69] activating sirtuin-1 enzymes in pancreatic beta cells for glucose stimulated insulin release,[70] reactivation of nicotinamide phosphoribosyl transferase enzyme for NAD^+ biosynthesis involved in glucose stimulated insulin secretion in islet cells,[71] and mitochondrial activity restoration in various aging related diseases.[72−74] Current invasive methods such as immunohistochemistry, metabolic assays, and polymerase chain reaction (PCR) are currently used to measure cell metabolism both *in vitro* and in tissues to determine NAD^+ regulation in cells. These techniques are laborious and tissue destructive, often rendering cells unviable and unrecoverable, making it incompatible with *in vivo* dynamic observations. We report a noninvasive optical technique to monitor the upregulation of NAD^+ in keratinocytes (*ex vivo*) upon administration of NMN coated solid μNDs. By exploiting the intrinsic autofluorescence of cells and tissues using multiphoton microscopy, we demonstrate that fluorescence of the endogenous NADH in the keratinocytes shows decreased average fluorescence lifetime (τ_m) and the free unbound NADH (τ_1) on NMN coated μND treated mouse skin *ex vivo*. Using this innovative μND platform, we show a promising, minimally invasive alternative delivery system for the NAD^+ precursor molecule that can enhance patient compliance and therapeutic outcomes.

2. MATERIALS AND METHODS

2.1. Materials and Equipment. All μND arrays were printed from a UV-curable resin (eResin-PLA Pro Transparent, eSUN), fluorescein was purchased from Sigma (F7505), sucrose was

https://doi.org/10.1021/acsbiomaterials.4c00905
ACS Biomater. Sci. Eng. XXXX, XXX, XXX−XXX

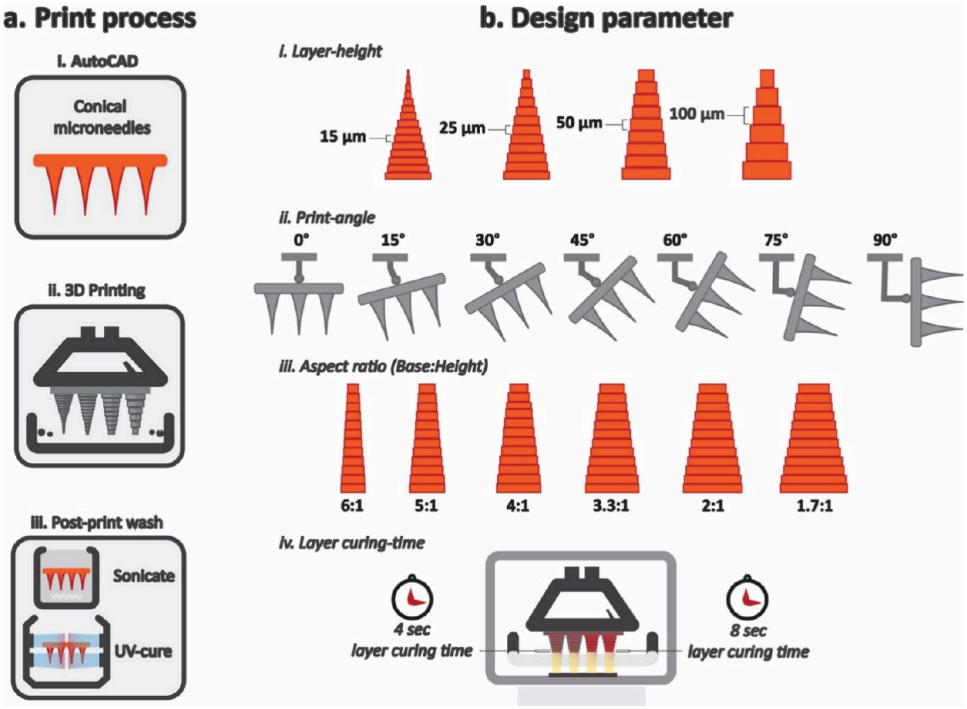

Figure 1. µND design parameters examined in the 3D printing process. (a) 3D printing process involving designing the µND in an AutoCAD (i) and then transferring the design file to the 3D printer for printing (ii) followed by postprint washing and UV-curing (iii). (b) µND 3D printing design parameters explored were print layer-height (i), print-angle (ii), aspect ratio (iii), and layer curing-time (iv).

purchased from Ajax Finechem (342.3 g/mol, 0809450), carboxymethyl cellulose (CMC) was purchased from Sigma (high viscosity: 419273 and low viscosity: C5678), Tween-20 was purchased from Sigma (P2287), and NMN was purchased from Agemate (Melbourne, Australia).

Full thickness human donor skin was donated from patients undergoing abdominoplasty at Brisbane hospitals (Australia). Ethics approval was granted by The University of Queensland Human Research Ethics Unit, approval number: 03081 (HREC/16/QPAH/64). After collection, subcutaneous fat was removed by a scalpel blade, and then skin was frozen at −80 °C for further use.

2.2. 3D Printer Parametric Study. *2.2.1. 3D Printing and µND Design Parameters.* The design parameters to print high fidelity µNDs used in this study were already studied elsewhere.[34,38,39] However, to better understand the limitations of the PHROZEN 3D printer, we systematically performed proof of concept experiments with the following design parameters diagrammatically illustrated in Figure 1b. The µND array CAD design files were exported to STL file format and imported into print preparation software (ChiTuBox V 1.3.0) (Figure 1a-i). The printing was carried out using a low-cost desktop 3D printer (4K Sonic Mini Phrozen, China; Figure 1a-ii). The body of the µND prototype was orientated so that the center axis of the needles aligned with the *z*-axis of the printer. After 3D printing, the finished µND array models were washed using ultrasonication in a methanol bath for 4 min followed by a detergent wash for an additional 4 min (Figure 1a-iii). After washing, the needles were cured for a total of 8 min using ultraviolet light emitting diodes (UV LEDs, λ = 405 nm) at 4 min intervals (Phrozen curing chamber).

All designs were 4 × 4 arrays of conically shaped µNDs with a 5 mm interneedle distance. Experiments were systematically conducted to determine the appropriate printing conditions that would yield the most accurate outcome. To determine the 3D printer print quality, µNDs were designed with input height of 1.8 mm, input base diameter of 0.8 mm, print layer curing height of 100 µm, and modifying the polymer resin by including an additive (methanol). This was performed to investigate the accuracy of the 3D printers' print quality on both the original and modified resin. To determine the ideal 3D printer print-layer height that would yield a smoother µND surface, µNDs were designed with input print-layer heights of 15, 25, 50, and 100 µm (Figure 1b-i), with µND input height of 1.2 mm and input base diameter of 0.8 mm. To determine the ideal print angle, the µNDs were designed with input print angles from 0−90° in increments of 15°, with µND input height of 1.2 mm and base diameter of 0.4 mm (Figure 1b-ii). To determine the ideal µND print aspect ratio, µND arrays were designed at six different aspect ratios (6:1, 5:1, 4:1, 3.3:1, 2:1, and 1.7:1), and for each respective aspect ratio, µND arrays were printed with varying needle base diameters (167, 200, 250, 300, 500, and 600 µm), while the µND height was constant at 1.0 mm (Figure 1b-iii). The last design parameter was the print-layer curing time (Figure 1b-iv). µND arrays were designed with nine varying needle height × base (1000 × 588, 900 × 529, 800 × 470, 700 × 411, 600 × 353, 500 × 294, 400 × 139, 300 × 176, and 200 × 117 µm), and for each µND array two curing times were explored (4 and 8 s print-layer curing time).

2.2.2. µND Inspection. A Zeiss Stemi 2000-C stereomicroscope with a stand-alone Axiocam ERc 5s microscope camera (Zeiss, Germany) was used to image µND arrays. The microscope was connected to the computer and run by Axiovision 4 LE viewfinder app to capture images and make iterations such as interactive geometric measurements, scale magnification, and scale units. Additionally, µND arrays were also visualized on a benchtop scanning electron microscope (Jeol NeoScope JCM-5000, SEM), by placing them on circular discs and scanning them in high-vacuum mode using the Everhart−Thornley detector (ETD) at 10^{-5} Torr and 15 kV. After initial visual inspection, parameter dimensions were approximated by performing an analysis on digital images of samples taken with the microscope.

2.3. µND Coating and Skin Deposition Visualization. *2.3.1. Coating Formulation Optimization.* Our study aimed at investigating the physical chemistry of the coating formulations to (a) examine the effects of coating formulation excipients on the mass of drug coated onto µNDs, (b) develop strategies using 3D printed coating tank prototypes in order to achieve coating uniformity and thickness on µNDs, and (c) deliver drug formulations using 3D printed solid µNDs. To accomplish these objectives, we first optimized the physical properties of the coating formulation to

https://doi.org/10.1021/acsbiomaterials.4c00905
ACS Biomater. Sci. Eng. XXXX, XXX, XXX−XXX

control the fluid mechanics of the coating process using two different coating tank prototypes for the dip-coating technique, which was then followed by exploring the μND surface wetting properties.

The Young equation (eq 1) generally governs the wetting of a solid surface with a liquid under static conditions, and the contact angle should be zero for the liquid to uniformly spread on the solid surface to form a uniform liquid film.[75]

$$\gamma^{SV} = \gamma^{SL} + \gamma^{LV} \cos(\theta c) \quad (1)$$

The surface tensions of the solid−vapor, liquid−vapor, and solid−liquid are denoted by γ^{SV}, γ^{LV}, and γ^{SL}, respectively. The surface tension between two materials when in contact is denoted by γ^{SL} forming the contact angle θc.

Guided by these physical principles, this study examined the effect of coating solution surface tension and viscosity on μND surface modification, specifically looking at the μND coating uniformity and the mass of drug coated on μNDs. The coating solution surface tension was optimized by the addition of surfactant and by using nonaqueous solvents and the addition of a viscosity enhancer to increase the coating thickness to coat larger amounts of therapeutics onto the μND surface.

2.3.1.1. Coating Solution Formulations. The aqueous coating solution formulations (w/v % unless otherwise specified) were prepared using Milli-Q water according to Table 1.

Table 1. Formulations Prepared for the Coating Solutions and Their Excipients

formulation	fluorescein (mg/mL)	NMN (mg/mL)	viscosity enhancer	Tween-20 (v/v %)
A	2	-	sucrose (5 mg/mL)	0.01
B	2	-	sucrose (50 mg/mL)	0.01
C	2	-	CMC (1% low MW)	0.01
D	2	-	CMC (1% high MW)	0.01
NMN	-	50	sucrose (5 mg/mL)	0.01

2.3.1.2. Coating Solution Fluorescence and Contact Angle Measurement. Fluorescence of the aqueous coating solution containing sucrose and CMC was measured using a Thermofisher spectrophotometer (Multiskan) (excitation spectrum was 545 nm, and emission spectrum 570 nm). Static advancing contact angles of the coating formulations containing various excipients were measured on a 3D printed plate (to mimic the μND surface) using a high-resolution camera setup to capture the droplet at zero degrees and calibrated for surface vibration and room temperature (Figure S1). Both the fluorescence and the contact angles were measured at room temperature with a sample size of $n = 5$ for each solution.

2.3.1.3. Effect of Coating Solution's Surfactant and Viscosity Enhancer. To study the significance of surfactant and viscosity enhancers in producing uniform coatings on the 3D printed μNDs, μND arrays ($n = 3$) were dipped in formulations A−D (containing fluorescein). Additionally, aqueous solutions of individual constituents in formulations A−D with fluorescein (2 mg/mL) were also used to evaluate their relative and synergistic effects, as well as to assess the ability of both the surfactant and the viscosity enhancers to produce uniform coatings. Coated μNDs were air-dried for 2 h and examined by fluorescence microscopy using an Olympus IX73 fluorescence microscope (Olympus America, Center Valley, PA, USA) to assess coating uniformity.

Evaporation of the coating solutions (formulations A and D and formulation NMN) during the coating of the μND arrays was also investigated. This was performed using gravimetric analysis of the coating formulation weight loss over 90 min (total time for the coating experiment). Surface tension measurement was performed following an established method,[76] using axisymmetric drop shape analysis with a pendant drop tensiometer (OCA-15EC, DataPhysics Instruments, Germany) following the Young−Laplace fitting.

2.3.2. Preparation of Coating Tanks for Coating 3D Printed μNDs. To ensure the uniformity of coating on 3D solid μND arrays, two different coating prototypes were 3D printed based on the dip coating technique. The first prototype coating tank (Figure 2a) was 3D printed similar to those in refs 62 and 67 with some modifications. The dimensions of the coating tank are height 10 mm and inner dimension 7 × 7 mm with a small housing to place the μND ring with dimensions 6 × 6 mm and 300 μm in depth from the top of the tank, and approximately 500 μL of coating solution was filled into the tank that reached the red continuous line shown inside the coating tank in Figure 2a. A square spacer approximately 300 μm in height and with dimensions of 5 × 5 mm was 3D printed. This spacer creates a barrier for the coating solution to coat the base of the μND (Figure 2a). The second prototype coating tank was 3D printed (Figure 2b) with the aim of creating microtanks on a flat base that would facilitate the immersion of individual μND tips only for the coating process. The

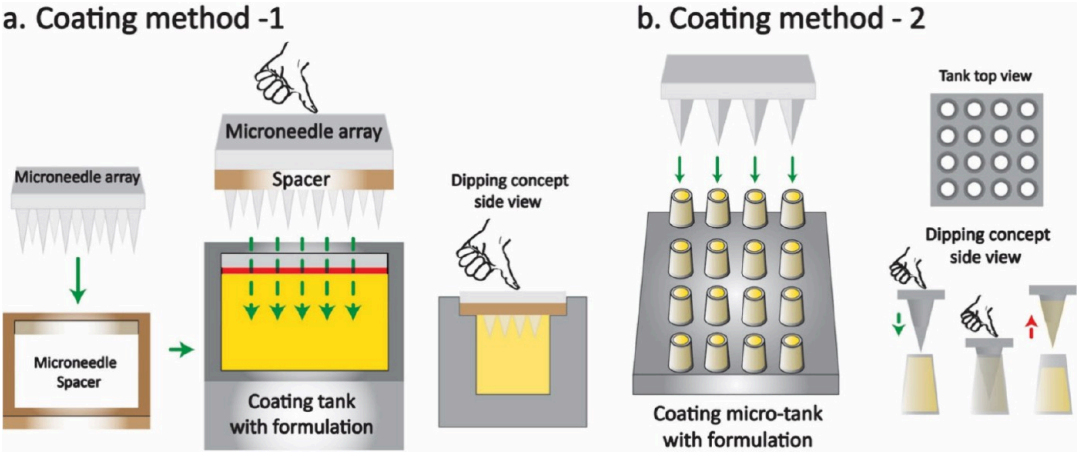

Figure 2. Illustrations of the two coating strategies used in this experiment. (a) Coating method 1 showing the various 3D printed parts which include the μND array, the μND spacer, assembling the μND array and the μND spacer, and the coating tank containing the coating formulation. The μND spacer acts as a stopper (marked as a red line in the coating tank) that is approximately 300 μm from the top of the coating tank, and this is to stop the coating solution from reaching the base of the μND. (b) Coating method 2 showing the various 3D printed parts which include the μND array, the specialized coating tank containing microtanks (4 × 4), and an illustration demonstrating a single μND fitting inside a microtank which does not reach the bottom of the μND base.

https://doi.org/10.1021/acsbiomaterials.4c00905
ACS Biomater. Sci. Eng. XXXX, XXX, XXX−XXX

dimensions of the individual microtanks were as follows: microtank inner diameter 500 μm and height 1.2 mm, 4 × 4 microtank array with the distance between the microtanks set as 4 mm (space between two individual microtanks). As illustrated in Figure 2b, the microtanks are open from both ends to facilitate the filling from the back of the base rather than the top to avoid coating solution transfer onto the μND base. The dimensions of μNDs utilized for the coating experiments are height 800 μm and base diameter 500 μm. Approximately 64 μL (4 μL × 16 microtanks) of the coating solution was used to fill the entire array of microtanks. These dimensional parameters ensure a perfect fit on the respective coating tanks to avoid any coating on the base plate of the μND array. For the coating process, the μNDs were first aligned with the microtanks filled with coating solution followed by immersion of μND shaft into the microtanks. The μND shafts were kept in the microtanks for 5 s. The μNDs were then removed and kept inverted (μNDs facing downward) for drying at room temperature under vacuum for 5 min. This microtank-based coating process was repeated multiple times (3, 5, 7, 9, or 27 times) for coating optimization.

2.3.3. Mechanical Integrity of Uncoated and Coated NMN 3D Printed μNDs. Compression studies on both uncoated and coated NMN 3D printed μND arrays were performed following an established method,[77] with slight modification. Briefly, compression studies were performed using a texture analyzer (CT3 Texture analyzer, Brookfield). Prior to compression, μND shaft heights were visualized using a Zeiss Stemi 2000-C stereomicroscope. μND arrays (±NMN) were placed between compression plates of the texture analyzer device. The compression rate was set at a speed of 0.05 mm/s, with a trigger force of 0.05N, moving a distance of 0.4 mm, operated at room temperature (22−24 °C). Compressive strength of the respective μND arrays was determined by measuring displaced distance as the tested μND sample was compressed at an applied axial force.

2.3.4. Cell Cytotoxicity Test. All cytotoxicity studies were performed using human immortalized keratinocyte cell line HaCaT (RPMI 1640 medium, ThermoFisher Scientific, Massachusetts, USA), following a protocol recommended by the American Type culture Collection (ATCC), which was described elsewhere,[78−80] while assessing the cytotoxicity of 3D printed μNDs followed another established protocol.[81] Briefly, the human immortalized keratinocyte cell line, HaCaT (RPMI 1640 medium, ThermoFisher, Australia), was maintained in Roswell Park Memorial Institute (RPMI) 1640 medium with 10% fetal bovine serum (FBS) and 1% antibiotics (10,000 μg/mL streptomycin and 10,000 units/mL penicillin) in a humidified chamber at 37 °C with 5% CO_2. When cells were 80−90% confluent, old medium was discarded, and cells were gently washed with 1× Dulbecco's phosphate-buffered saline solution (GIBCO, ThermoFisher Scientific, Massachusetts, USA) and detached with Trypsin-EDTA (Sigma-Aldrich, USA). RPMI full medium was added to inactivate the Trypsin-EDTA after cell detachment. The cells were then centrifuged, resuspended in the RPMI culture medium, and seeded onto 96-well plates (Corning Inc., Corning, NY) at 10^5 cells/well with 100 μL of RPMI medium and left in an incubator at 37 °C and 5% CO_2 for 24 h, for the cytotoxicity assays. Discs (diameter: 5 mm, thickness: 0.5 mm) of cured methacrylate resin (identical to μND fabrication) were 3D printed and washed as per section 2.2.1. After 24 h, the medium from the seeded cells was aspirated and supplemented with 100 μL of fresh RPMI media. The discs were then put in contact with the cell monolayer by placing them gently into the respective wells, for both 24 and 48 h. The cell cytotoxicity assay followed ISO 10993 for the biological evaluation of medical devices,[82] by placing a piece of the tested material in direct contact with the cells while growing. A cell-free group was used as blank, and cells with no material treatment were used as control, while cells with washed μNDs were used as samples.

After 24 and 48 h of treatment, 20 μL of ab112118 solution (Cell Cytotoxicity Assay Kit, Cambridge, UK) per well was added in each group, and the plates were incubated for 4 h at 37 °C and 5% CO_2. The samples were detected with a Thermofisher spectrophotometer (Multiskan) microplate reader at a wavelength of 570 nm. The optical density (OD) values of the blank (OD_b), control (OD_c), and sample (OD_s) groups were recorded, and the cell viability was calculated using eq 2:

$$\text{Cell viability (\%)} = \frac{OD_s - OD_b}{OD_c - OD_b} \quad (2)$$

2.3.5. μND Skin Insertion. To visualize the coating efficiency on the 3D μNDs, the coating solution was slightly modified, with Rose Bengal (RB) dye included instead of NMN. 3D printed μNDs with dimensions of 800 μm (needle height) were used for this study. Fluorescence microscopy (Olympus IX73) was used to visualize the RB coated 3D μNDs. The laser was set to 561/570 nm for excitation/emission maxima and constant for all experiments. To visualize the depth of insertion using confocal laser scanning microscopy (CLSM), the RB coated 3D μND array was inserted into excised human skin *in vitro* using a gentle push by thumb and then holding for 45 s. Following that, the μND array was removed from the skin and mounted on a microscopy slide with a coverslip. Olympus Fluoview FV3000 Multilaser confocal microscope (USA) was used for this study, imaging an area large enough to cover 4 holes made from the one section of the μND array in one tiled image. The ideal excitation wavelength of RB dye is 559 nm, and the emission peak is at 571 nm;[83] however, due to instrument related constraints, the laser in the Olympus Fluoview was set to 545 and 640 nm for excitation with the power set at 6.8 mW, constant for all experiments (z-height). The images were generated over 10 layers in depth at a step of 15 μm/depth. The *z*-axis profile of the intensity depth was used to determine the top layer of the skin sample.

Scanning electron microscopy (SEM) was also used to verify the skin puncture (micropore) created by the NMN μND arrays. Examinations of the puncture profiles of the μND array treated full thickness skin was taken with the Hitachi SU3500 (Tokyo, Japan) using a secondary electron detector with the accelerating voltage set at 10−15 kV, high vacuum, and spot size set to 35.

Skin membrane disruption and micropore was determined using histology cryosectioning and Scanning electron microscopy (SEM), respectively. 3D printed μND arrays with/without NMN load were used for this study. The μND array was applied onto excised human skin using a Texture Analyzer (CT3 Texture analyzer, Brookfield), at a speed of 0.5 mm/s and force of 20 N and held for 45 s, modified from ref 84. For histology cryosectioning, the μND insertion area was excised using a scalpel, placed in cryostat molds, and embedded in optimum cutting temperature (OCT) media (Sakura Tissue-Tek, Torrance, USA). The skin was fixed in OCT by freezing the sample on dry ice, then sectioned at 20 μm, and mounted onto Superfrost Plus glass microscopy slides (Menzel-Gläser, Germany, Braunschweig). This was followed by fixing for 1 min in 10% neutral buffered formalin then washing in water immediately prior to staining. Hematoxylin and eosin (H&E) staining was performed on a Tissue-Tek Prisma Autostainer, where slides were stained with Harris Haematoxylin (Australian Biostain P/L, Australia) for 5 min, washed in running tap water for 4 min, differentiated in acid alcohol (1% v/v) for 10 s, washed and blued in running water for 5 min, stained in 1% Alcoholic Eosin Y (ProSciTech, Australia) for 1 min, dehydrated in 1 station of ethanol (80% v/v), and 2 changes of 100% ethanol (2 min each) and cleared in 3 changes of xylene (2 min each). Slides were automatically coverslipped by the attached Tissue-Tek Glas coverslipper using Tissue-Tek Glas Mounting Media (Sakura Finetek, USA).

2.4. *In Vitro* Release and *In Vitro* Permeation Test.

2.4.1. Pharmaceutical Analysis of NMN. NMN was quantified using a high-performance liquid chromatographic (HPLC-UV) system (Shimadzu, Japan). NMN has an absorption maximum at 254 nm.[85] Ten concentrations (100, 50, 25, 12.5, 6.25, 3.125, 1.5625, 0.78125, and 0.390625 μg/mL) were prepared by serial dilution from a stock NMN solution of 200 μg/mL, using water as the solvent. HPLC conditions were developed as per an established protocol.[85] The conditions are briefly outlined as follows: HPLC-UV (Shimadzu, Binary Pump, Shimadzu Standard Autosampler, Shimadzu Variable

https://doi.org/10.1021/acsbiomaterials.4c00905
ACS Biomater. Sci. Eng. XXXX, XXX, XXX−XXX

Wavelength Detector, Japan) with UV detection set at 254 nm, Agilent eclipse column-C18 3.5 μm, 4.6 × 150 mm, with a column guard (AJ0-6071, Phenomenex) of matching chemistry was used for the analysis; mobile phase was acetonitrile (10% v/v) with a flow rate of 0.5 mL/min, and a run time of 8 min per sample; injection volume was 20 μL. The chromatograms obtained were analyzed using Shimadzu LC solutions Software (1.25 SP5).

NMN standard, sucrose, Tween-20, coating solution (with NMN 400 μg/mL) and NMN coated μNDs (5 dip coating) were subjected to chromatographic (HPLC) and mass spectrogram (LC-MS) analysis. The LC-MS/MS system consisted of a Sciex API 5000 triple quadrupole mass spectrometer (Framingham, MA, USA) equipped with a Shimadzu HPLC pump (LC-20AD, Shimadzu) and an autosampler (Shimadzu). The analytes were separated by an Agilent eclipse column-C18 (3.5 μm, 4.6 × 150 mm) column operated at 24 °C with a mobile phase consisting of acetonitrile (20% v/v). The chromatography was run isocratically with a run time of 8 min. The injection volume was 10 μL, and the flow rate was 0.5 mL/min. The mass spectrometer was operated in positive ion mode with an electrospray and MRM scan.

2.4.2. Coated NMN Permeation Test. The *in vitro* NMN skin permeation from the coated μND array treated skin was studied using the vertical Franz diffusion cell technique using a modified technique from refs 86 and 87. Briefly, donated human skin portions *in vitro* were processed (fat removed) to final thickness of approximately 2 mm, then cut into appropriate size (1.33 × 1.33 cm^2) to fit into the donor compartment of the Franz diffusion vertical system. The skin portion was then mounted onto the receptor compartment of the Franz diffusion cell with the stratum corneum (SC) side facing upward. Two replicates each from 3 different skin donors were used. After mounting the skin, the receptor compartment was filled with PBS (0.05% (v/v) NaN_3), and the cells were equilibrated in a water bath for 30 min and thermostatically maintained at 35 ± 1 °C with continuous stirring using magnetic stirrer bars to maintain a skin surface temperature of 32 °C. The integrity of the skin membrane was assessed by measuring the resistance between the donor and the receptor compartment with Ag/AgCl electrodes attached to a multimeter (Digitor Q1563, DSE, Brisbane, Australia). Skin that showed resistance lower than 20 kΩ·cm^2 was discarded. The receptor compartment was then emptied, and the skin membrane surface was wiped gently with KimWipes from Kimberly-Clark, Brisbane, Australia. After refilling the receptor compartment with fresh PBS (0.05% NaN_3, 0.5% Brij O20), Brij O20 was added to enhance the solubility of the permeating actives in the receptor fluid. The skin was transiently removed from the receptor chamber and placed onto an absorbent paper with SC side upward, followed by application of the NMN coated μND array on the skin SC side by gentle push of the thumb and holding for 45 s. The μND treated skin was then returned to the receptor chamber, followed by placing the donor compartment on top of the receptor compartment and securing it tight. The donor cell was unoccluded, except a small bob was placed atop the μND array to stop it from detaching from the skin. Sample collection points were every 15 min for the first hour, then at 2, 4, 6, 12, and 24 h. To determine the NMN content, samples were filtered through 0.5 μm filter and injected into the HPLC-UV system.

Additionally, the NMN content in the μND treated skin was quantified by the tape strip method with slight modifications.[88] Briefly, after the completion of *in vitro* permeation studies, the skin was removed from the respective Franz diffusion cells. μND arrays were removed from the skin, and then tape strips were applied on the surface of the skin and stripped off. This process was repeated 20 times, collecting 20 strips in total. The strips were pooled, along with the used μND arrays, then the NMN was extracted in water overnight at room temperature to ascertain the amount of NMN in the skin (tape strips) and μND array.

2.5. *Ex Vivo* Determination of NAD^+ from NMN μND Arrayed Skin. NMN coated μND arrays (5× dip coated NMN μND arrays only) and coated μND arrays without NMN (control) were used to determine the synthesis of NAD^+ and NADH in *ex vivo* mouse ear skin. The arrays (n = 2) were applied onto a freshly excised full thickness skin (n = 4 donors). The arrays were pressed gently (approximately 10 g load) onto the skin for 5 min. Following this, the arrays were removed and visually verified (light microscopy) for the dissolution of the microprojections. Any residual polymer on the stratum corneum was gently cleaned, and then the skin placed on a glass slide for multiphoton imaging.

The endogenous autofluorescence of the epidermis was imaged using the multiphoton tomography (MPT) DermaInspect (JenLab GmbH, Jena, Germany), from a previously established protocol.[89] . Briefly, the imaging system consists of Plan-Neofluar high-NA oil-immersion 40×/1.30 objective lens (Carl Zeiss, Germany). The light for excitation was provided by the ultra-shortpulsed, mode-locked, 80 MHz, titanium sapphire laser (Mai Tai, Spectra Physics, Mountain View, California, USA) with a tuning range of 710−920 nm and an 85 fs pulse width. The endogenous cellular autofluorescence of NAD(P)H was imaged by using an excitation wavelength of 760 nm (two photon), at an optical power of 23 mW and at an exposure of 47 s with an acquisition image size of 512 × 512 pixels (256 × 256 μm^2). A bandpass filter of 350−650 nm (BG39, Schott glass color filter) was used to optically filter the emitted fluorescence light to capture live images of MPT or toward the fluorescence lifetime imaging microscope (FLIM) detectors. In front of FLIM detectors, 350 to 450 nm (channel 1) and 450 to 515 nm (channel 2) band-pass filters were used to isolate NAD(P)H signal into separate channels. FLIM measurements were carried out by using a time-correlated single-photon counting SPC-830 detector system (Becker & Hickel, Berlin, Germany) integrated to the multiphoton microscopy. This FLIM system builds a photon distribution at the x and y coordinates of the scan area for each photon detected and determines its time of arrival within the fluorescence decay. In this way, an averaged image with data pertaining to the lifetime of the fluorophores is generated. We acquired FLIM images of the stratum granulosum and stratum spinosum layers at a specific depth determined by keratinocyte morphology.[90,91] FLIM images are based on the arrival times of single photons for different fluorescent solutes after a given excitation pulse (760 nm), consequently building up a photon distribution for each pixel in the scanned area. Our FLIM data is modeled assuming a biexponential decay, eq 3:

$$f(t) = a_1\, e^{-t/\tau_1} + a_2\, e^{-t/\tau_2} \text{ with } a_1 + a_2 = 1 \tag{3}$$

where a_1 and a_2 are the amplitudes and τ_1 and τ_2 are the fluorescence lifetimes of the fast (τ_1, $NADP^+$) and slow (τ_2, NADPH) decay components, respectively.[90,91] The instrument response function of each FLIM image generated is convoluted with model function $f(t)$ to obtain the function $F(t)$ or a decay curve. The decay curve is then fitted to each measured pixel to calculate and create a color coded image of each decay parameter. Additionally, the intensity fractions a_1 and a_2 are the pre-exponential variable associated with the τ_1 and τ_2 lifetime components of the biexponential decay profile on a per pixel basis.[90−92] a_1% and a_2% are normalized variables according to eq 4, which are then used in eq 5 to calculate the average fluorescence lifetime (τ_m):

$$a_1\% = \frac{a_1}{a_1 + a_2} \text{ and } a_2\% = \frac{a_2}{a_1 + a_2} \tag{4}$$

$$\tau_m = \frac{[(\tau_1 X a_1\%) + (\tau_2 X a_2\%)}{a_1\% + a_2\%} \tag{5}$$

where τ_1 is NAD(P)H free nonenzyme bound lifetime, τ_2 is NAD(P)H enzyme bound lifetime, α_1% is the percentage of free nonenzyme bound fraction and α_2% is the percentage of enzyme bound fraction.

3. STATISTICAL ANALYSIS

All data are expressed as the average ± SD (Avg ± SD). Analysis of variance (ANOVA, one way or two way, Dunnett hypothesis test) was utilized to determine statistical significance. A p-value of <0.05 was considered statistically significant.

https://doi.org/10.1021/acsbiomaterials.4c00905
ACS Biomater. Sci. Eng. XXXX, XXX, XXX−XXX

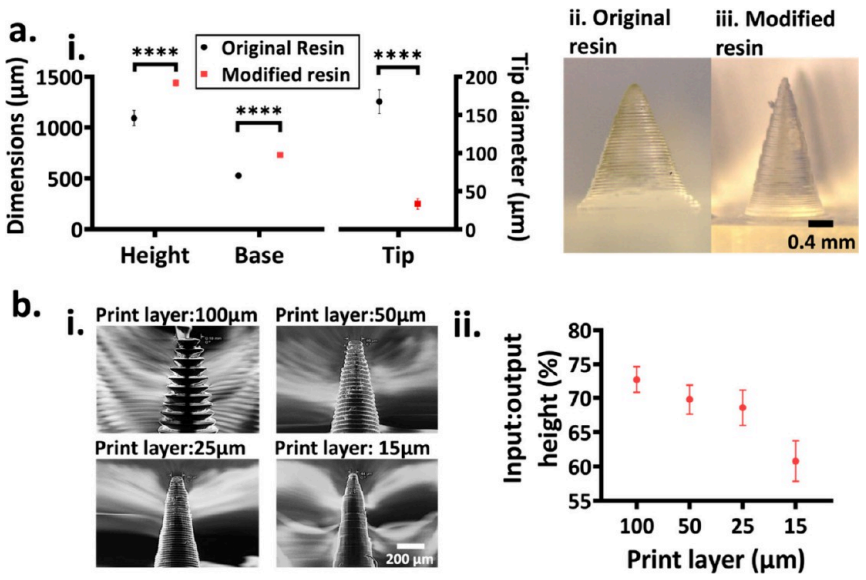

Figure 3. Resin modification and 3D printing accuracy studies. (a) μNDs were 3D printed using both the resins separately (original and modified); then their dimensional parameters such as (i) height, base, and tip diameter were assessed (n = 5, ****p < 0.0001 calculated using one-way ANOVA in PRISM; μND height = 1.8 mm and base diameter = 0.8 mm). Microscopy images of μNDs printed from original (ii) and modified (iii) resin, respectively. (b) (i) SEM images of 3D printed μNDs showing the four print-layer heights (100, 50, 25, and 15 μm). (ii) Quantitative analysis showing the input/output height % of needle height vs the four respective print-layer height (n = 3, input height 1.2 mm). Representative graphical data shows Avg ± SD, plotted in PRISM.

4. RESULTS

4.1. 3D Printer Optimization Study. First, a parametric study was conducted on printing needles using the low-cost desktop 3D printer optimizing print settings to produce the best possible μND geometry. The optimization study investigated the effects of print resin quality, print plate accuracy, varying print layer height and print angle, μND height/base aspect ratio, and print-layer curing time, and quantified print success by measuring three design parameters of the printed μNDs (needle height, tip radius, and needle base diameter).

4.1.1. 3D Printer Resin Modification. To produce μNDs with increased input to output ratio, first, the 3D printer resin quality (viscosity) was modified to a lower viscosity resin. This was performed to ensure that the light from the printer LED panel would sufficiently penetrate through the resin vat to create more intricate layers. To this extent, three experiments were carried out to test the efficacy of the modified resin: viscosity (rheometer), chemical composition (FTIR) and quantitative analysis of the dimensions of μNDs comparing μNDs printed using both the original and the modified resins. The polymer resin consists of methacrylate (monomer and oligomer), a photoinitiator, and a photo-cross-linker. Adding methanol as an additive reduced the viscosity of the original resin, while the carbonyl peak at 1700 cm^{-1} and ester peak at 1165 cm^{-1} remained unchanged (Figure S2). This modification improved the dimensional parameters of 3D printed μNDs (input μND height 1.8 mm, base diameter 0.8 mm, and print-layer curing height 100 μm) (Figure 3a-i), as more layers are visible thus increasing the μND height (Figure 3a=iii) compared to the native resin (Figure 3a-ii). However, the height of the 3D printed μND was 1439 ± 29.36 μm, making the output less than 79% of the input value still (height 1.8 mm) (Figure 3a-i). Furthermore, at 100 μm print-layer height, the "stair-stepping" phenomenon was visibly noticeable rendering the μND surface less smooth (Figure 3a-ii,b-i), which is quite common with DLP type 3D printers.[52]

Optimizing the 3D printer individual print-layer height during the printing process from 100 μm to 15, 25, and 50 μm (thickness of each cured layer in the z-direction) rendered a smoother μND surface (Figure 3b-i) due to the reduction in the layer height curing and thus reduced the "stair-stepping" phenomenon effect. This, however, resulted in a longer print time due to the addition of extra layers to attain the input height. Consequently, the needle height input/output % was quite low, i.e., 3D μNDs yielded 60.78 ± 2.970% and 68.59 ± 2.605% input/output at layer heights of 15 and 25 μm, respectively (Figure 3b-ii). Nonetheless, printing at 15 and 25 μm markedly reduced the edge ridge mismatches and removed the stair-stepping phenomenon.

4.1.2. Print-Angle and Aspect Ratio. While printing μNDs at 25 μm layer-height yielded a smoother needle surface, it did not improve the μND output height %. To improve the μND output height, we examined the effect of print angle whereby the μNDs were printed at various angles configuring both x- and y-axes. For this study, μNDs were designed with input height of 1.2 mm and base diameter of 0.4 mm, focusing on the effect of print angle on the output print quality. An increasing trend in the μND output height and a decreasing trend in the μND output tip diameter was observed with 3D printed μNDs when the spatial rotation of print angle increased (Figure 4a-i for spatial rotation images and Figure 4a-ii for quantitative data). μND height with the highest input/output ratio was printed at 90° at both x- and y-axes, yielding an output of 951.5 ± 31.62 μm (x-axis) and 1011 ± 25.90 μm (y-axis), compared to output at 0° (output: 676.6 ± 110.0 μm [x-axis only]), alluding to improved print quality (Figure 4a-ii). Similarly, printing μNDs at various angles produced sharper tips, yielding a tip diameter output of 52.63 ± 13.16 μm (x-axis) and 48.52 ± 10.43 μm (y-axis) (Figure 4a-ii). Upon changing the angle at which the 3D μNDs are printed, the needle input/output

https://doi.org/10.1021/acsbiomaterials.4c00905
ACS Biomater. Sci. Eng. XXXX, XXX, XXX−XXX

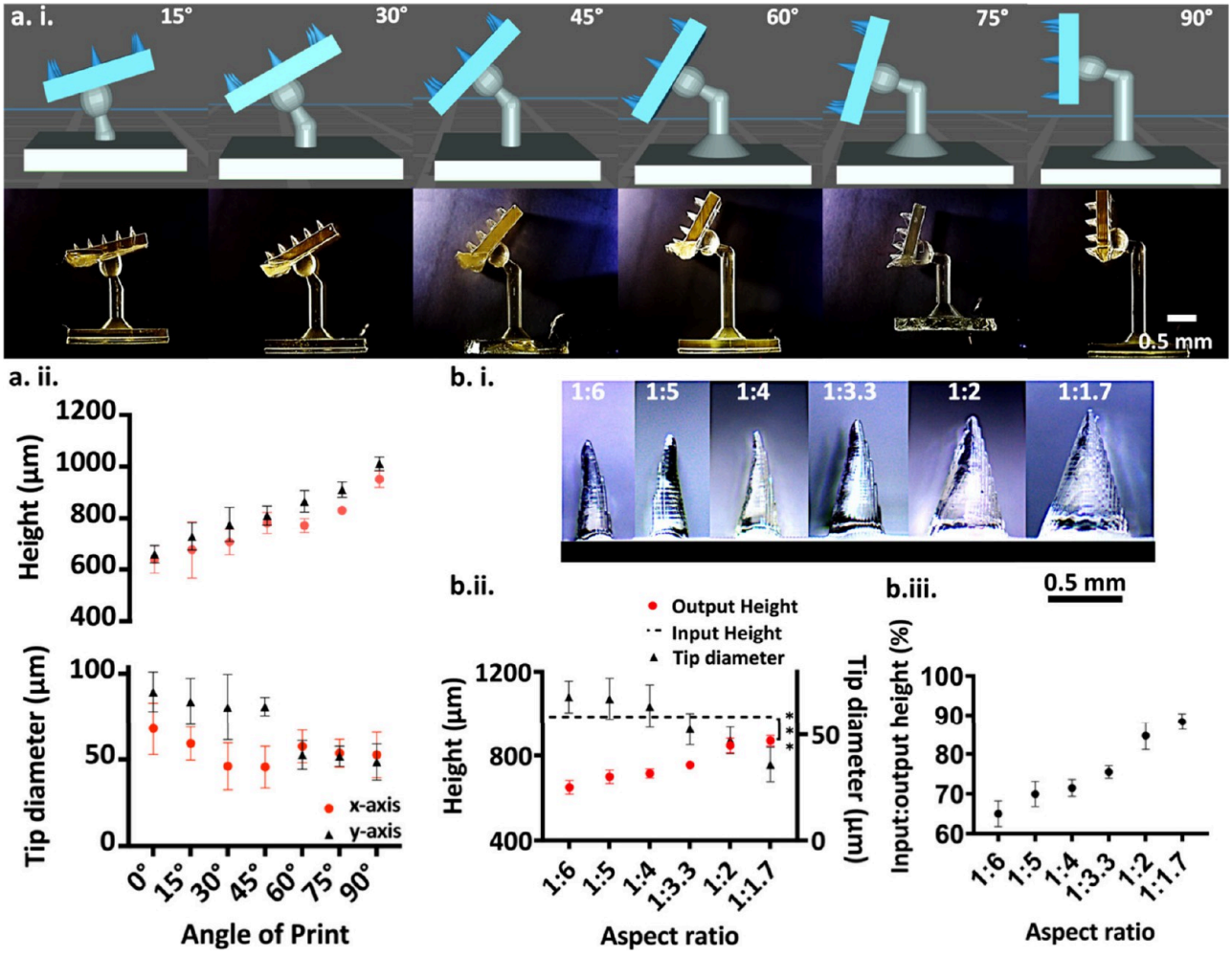

Figure 4. Effect of spatially adjusting 3D print angle and aspect ratio on μND height and tip diameter. (a) (i) Microscopy images (side view) of μND arrays (4 × 4) printed at various angles (0−90° at 15° increments per print). Illustration of change in print-angle is shown above the microscopy images, taken from the slicer software ChiTuBox. (a) (ii) μND height and tip diameter data printed at various print angles (n = 3, data shows Avg ± SD, plotted in PRISM) rotating the μND array at x and y axis. (b) (i) Microscopy images showing μNDs printed at various aspect ratios (1:6, 1:5, 1:4, 1:3.3, 1:2 and 1:1.7), with quantitative data of the output height and tip diameter (ii) and the input to output height % (iii) (n = 3, data shows Avg ± SD, plotted in PRISM; ****p < 0.0005 calculated using one-way ANOVA in PRISM).

height % also increased yielding 84.28 ± 2.158% of the input height (Figure S3). These data confirm that the spatial control of the print angle is critical for producing sharper μND tips with improved input to output height %. Choo et al.[54] also investigated the print angles when both x- and y-axes were simultaneously changed (our study only changed print angles on one axis per print). They demonstrated that when both axes were changed simultaneously, the μND tip morphology was circular and yielded sharper needle tips. They used a stereolithography based 3D printer with improved light processing technology (Formlabs, USA) equipped with its own 3D print slicer software to conduct their study. This was the limitation of ChiTubox 3D printer slicer software used in our study; i.e., the option of altering both axes simultaneously was unavailable in the software. Nonetheless, by altering the print angle of one axis per print, our study managed to produce μNDs with a tip diameter close to 48.52 ± 10.43 μm, which is sharp enough to be able to penetrate skin tissue.

To further improve the μND input to output height %, we investigated the effect of aspect ratio of the 3D printed μND height to base diameter ratio. The aspect ratio of μNDs is indicative of the structural mechanical strength (by reducing the aspect ratio or increasing the μND base diameter), typically giving it sufficient mechanical strength to penetrate the skin tissue. A recent study demonstrated that the experimental value for an ideal aspect ratio of the μNDs for successful skin penetration is between 2:1 to 10:1.[93] For our study, μND arrays of 4 × 4 were examined at various aspect ratios, changing the base diameter (167, 200, 250, 300, 500, and 600 μm) while keeping the μND height constant at 1.0 mm, yielding aspect ratios of 1:6, 1:5, 1:4, 1:3.3, 1:2, and 1:1.7 (Figure 4b-i). As seen in Figure 4b-ii, the relative difference between the input and output μND height significantly decreased (p < 0.005) with increased aspect ratio. This produced 11% shorter needles at an aspect ratio of 1:1.7 (88.37 ± 2.047%) compared to 35% shorter needles at aspect ratio of 1:6 (64.98 ± 3.219%) (Figure 4b-iii). At an aspect ratio of 1:1.7, the μND tip diameter was 36 ± 8 μm, further improving the tip sharpness.

We also examined the effect of print-layer curing time on 3D printed μNDs to see its effect on input to output height %. For this study, μNDs (4 × 4 array) were designed with nine varying needle height × base: 1000 × 588, 900 × 529, 800 × 470, 700 × 411, 600 × 353, 500 × 294, 400 × 139, 300 × 176,

https://doi.org/10.1021/acsbiomaterials.4c00905
ACS Biomater. Sci. Eng. XXXX, XXX, XXX−XXX

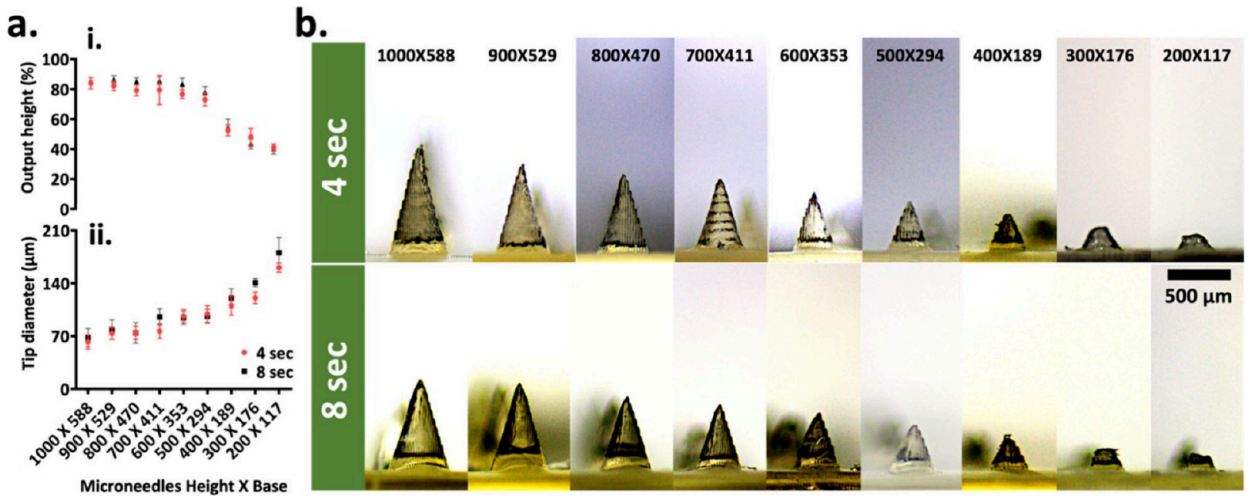

Figure 5. Effect of print-layer curing time of 3D printed μNDs on μND height and tip diameter. (a) μND output height and tip diameter % (i) and tip diameter (ii) data at various print-layer curing times (n = 3, data shows Avg ± SD, plotted in PRISM). (b) Microscopy images (side view) of μND arrays (4 × 4) printed at various needle height × base (1000 × 588, 900 × 529, 800 × 470, 700 × 411, 600 × 353, 500 × 294, 400 × 139, 300 × 176, and 200 × 117 μm); for each μND array, two curing times were explored (4 and 8 s layer-curing time).

and 200 × 117 μm, and for each μND array, two curing times were explored, 4 and 8 s layer curing time (Figure 5a,b). The 3D printer consistently produced μNDs above 80% of the input height in the needle height range 1000−500 μm at both 4 and 8 s layer curing time, then there was a sharp fall to 50% at 400 × 189 μm (Figure 5a-i). The decrease in the output height consequently affected the tip diameter (Figure 5a-ii), yielding blunt tips. This study also revealed the print-limitation of the Phrozen 3D printers. Although the manufacturer states that the print resolution of the 3D printer is 40 μm (laser spot size), the printer was unable to produce sharper needles at an output height of 400 μm (Figure 5b). Nonetheless, increasing the print layer curing time did not seem to increase the input to output ratio of 3D printed μNDs. 3D printed μNDs with dimensions of 800 μm (needle height) were used for subsequent experiments.

4.2. Cytocompatibility of 3D Printed μNDs. Cytocompatibility of 3D printed μNDs was investigated using HaCaT cells via the live/dead cell assay kit. 3D printed discs were used to test material cytocompatibility. To ensure material similarity between the discs and the μNDs, the discs were 3D printed in an identical manner to 3D printed μNDs. Further, this was also performed to maximize the material's surface area contact with keratinocyte cells without causing any cellular mechanical stress.[81] The results of the cytotoxicity test in Figure S4 show a decrease in cell viability of no more than 20% for cells grown with washed cured 3D printed discs for 24 h (86.52 ± 9.616%) and 48 (80.06 ± 9.036%). According to ISO 10993-5 (part 8.5 determination of cytotoxicity), a material is cytotoxic when there is a 30% reduction in cell viability.[82] Further, material cytotoxicity arises from the widespread use and incomplete wash of photoinitiators.[94−96] To ensure the safety of μND skin insertion while preventing inadvertent transfer of excess uncured resins, thorough rinsing of the μNDs was employed in our washing regimen.[97] Therefore, the washed μNDs are considered nontoxic even after 48 h of direct contact exposure, confirming that the efficacy of washing 3D printed μNDs demonstrated a neutral effect on cell proliferation as viability was steadily maintained at more than 80%.

A potential concern in our μND study is the possibility of allergic reactions due to residual solvents, unreacted monomers, or sensitizing agents present on the μNDs after fabrication. Although the materials used in this study may not be inherently cytotoxic, trace amounts of these substances could cause irritation, especially in individuals with sensitive skin or pre-existing allergies.[98,99] Even though past studies have emphasized the importance of thorough postfabrication cleaning and curing processes to minimize these risks,[97,100] the complete elimination of such residuals cannot be guaranteed, highlighting the need for careful consideration of material composition and fabrication methods to reduce the likelihood of adverse reactions.

Keratinocytes were selected for the cytotoxicity test due to their crucial role in the epidermis, the initial point of contact for μNDs, making them essential for assessing biocompatibility. These cells are reliable indicators of skin irritation and cytotoxicity, given their barrier function and responsiveness to external stimuli.[101,102] While fibroblasts and macrophages are also present in skin tissue, they are located in deeper layers (dermis and hypodermis, respectively) and are important for overall skin health and wound healing; the initial toxicity assessment is most effectively conducted on keratinocytes due to their direct exposure to μND application. This approach aligns with the common application of keratinocytes in toxicology studies, as their well-characterized response to chemical exposure[103] often makes them the preferred model for evaluating potential cytotoxic effects. Nonetheless, further cytocompatibility experiments with additional cell lines including fibroblast and macrophages, to assess immunological reaction,[104] as well as the FDA-approved excipients used to make the coating solution in our study, are warranted to ensure a comprehensive biocompatibility assessment.

4.3. Coating Strategies for 3D Printed μNDs. *4.3.1. 3D Printing of Coating Tank.* Two different coating tanks were investigated to study the coating efficiencies of 3D printed μNDs (Figure 6). Drop coating is a common applied method; therefore, it was tried initially; however, after dropping 2 μL of the fluorescein coating solution on the μND arrays (n = 3), the majority of the coating solution settled at the bottom of the needle, rendering it ineffective (Figure S5). To overcome the issue of coating on the μND base, coating tank prototype 1 was 3D printed (Figure 6a-ii,iii), where the μND spacer (5 × 5

https://doi.org/10.1021/acsbiomaterials.4c00905
ACS Biomater. Sci. Eng. XXXX, XXX, XXX−XXX

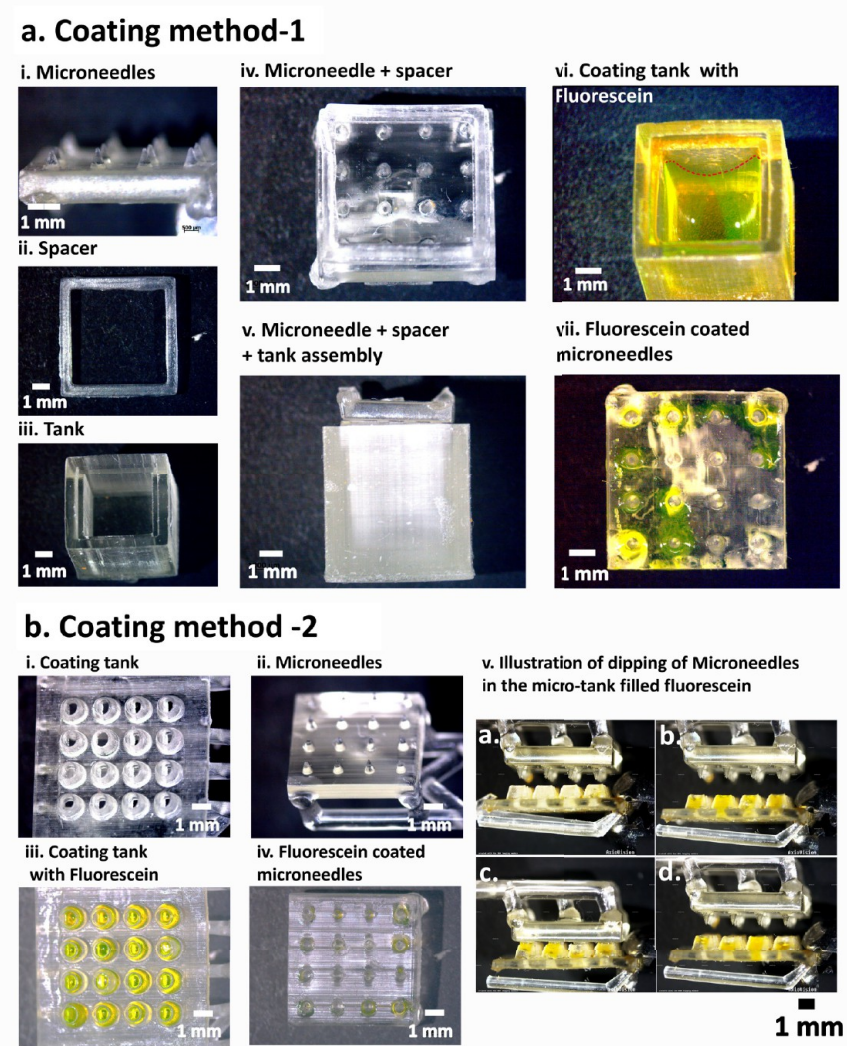

Figure 6. Coating strategies used in this experiment. (a) Coating method 1 demonstrating a 3D printed coating tank with a μND square spacer. Bright field images showing side view of μND array (i), Spacer (ii), and the 3D printed tank (iii), the Spacer placed on the μND array (iv), and then assembled on the tank (v). (vi) When fluorescein coating solution is placed in the tank, it forms a meniscus shown as red dotted line, which makes an uneven coating on the μND array (vii) contaminating the base of the μND. (b) Coating method 2 demonstrating only partial body of the μND tip being placed inside the microtanks. Bright field images of the coating tank containing 16 microtanks (i) and fluorescein filled microtanks (iii). When μNDs (ii) are dipped inside the microtanks (illustration in v), the evenness of the coating concentrated to the μND shaft is concentrated on the tips only (iv). (v, a–d) Illustration of the dipping of μNDs into the fluorescein filled microtanks.

mm^2, Figure 6a-ii) was hypothesized to stop the coating solution from reaching the base of the μND array, as illustrated in Figure 6a-iv,v. However, due to the hydrophilicity of the coating solution which increased its surface tension, the volume of coating solution height was higher around the tank's side walls (indicated by red dotted line, Figure 6a-vi), thus coating the μND arrays around the edges of the base (Figure 6a-vii), rendering it ineffective.

To ensure that the coating solution forms a coating-film layer only on the μND tips and not the base, coating tank prototype 2 was 3D printed (Figure 6b-iii) which included individual microtanks on a base plate with the dimensions of the microtank only facilitating the coating of the μND shaft (Figure 6b-i,iii). The individual microtank dimensions were 400 μm (diameter of microtank opening) and 1.2 mm in height, such that when μND array of dimension 800 × 500 μm (height × base diameter) (Figure 6b-ii) was dipped into the microtanks (Figure 6b-v), the coating solution did not reach the base of the μND array (Figure 6d-iv). To date, this is the first study to report on the fabrication of on-demand miniaturized 3D printed microtanks for the coating process. Two other studies[66,67] demonstrated the dip coating method using coating tanks similar to Figure 6a (minus the μND spacer); however, our study showed variable results with that technique, contaminating the μND base with the coating solution (Figure 6a-vii).

4.3.2. Effect of Coating Solution's Surface Tension and Viscosity. The two critical factors determining μND coatings are dose reproducibility and high drug loading onto the μND surface. This requires the precision deposition of uniform and thick coatings onto μND shafts. Control over physical properties and kinetic parameters that affect the thermodynamics and hydrodynamics of dip-coating is expected to result in uniform and thick coatings. Additionally, surface tension and viscosity are the two physical properties of the dipping formulation that are known to influence the thermodynamics and hydrodynamics of dip-coating. However, the complex physics of dip-coating is not fully understood to develop

https://doi.org/10.1021/acsbiomaterials.4c00905
ACS Biomater. Sci. Eng. XXXX, XXX, XXX−XXX

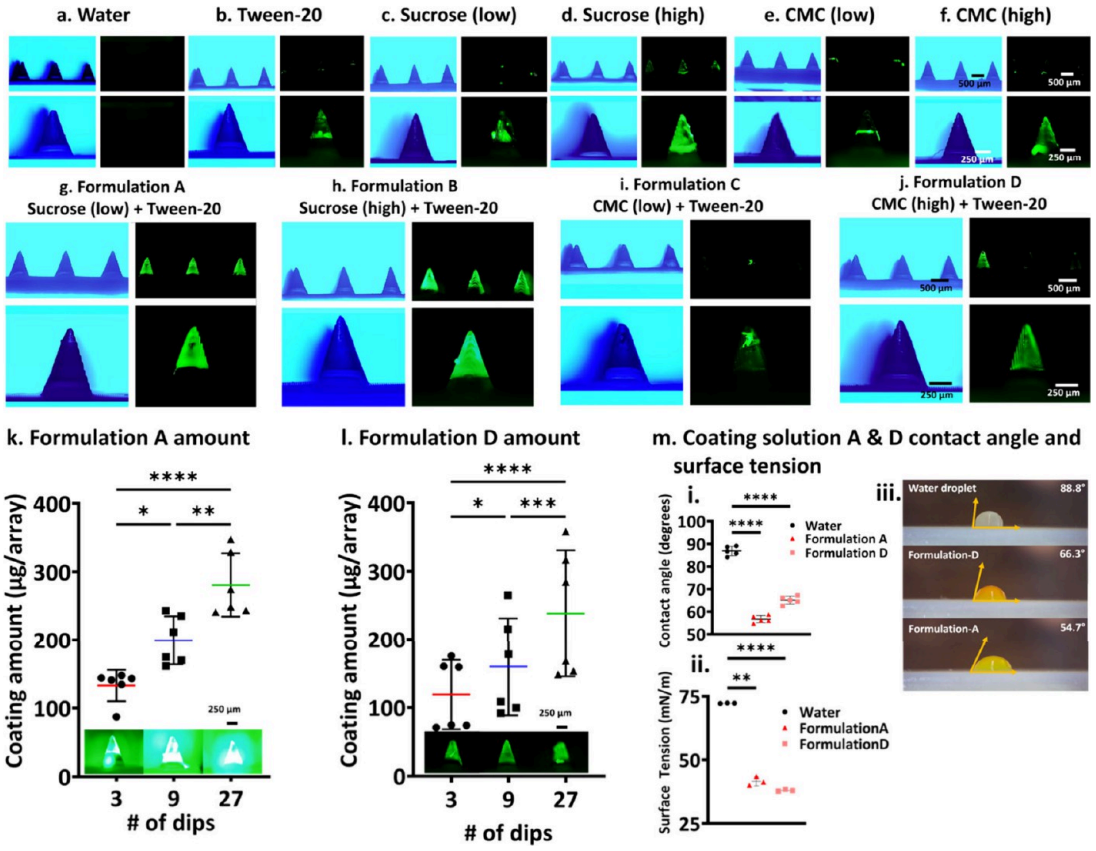

Figure 7. Effect of surface tension and viscosity on coating uniformity on μNDs with fluorescein as the model drug. Bright field illumination images with supplemental fluorescence microscopy images showing μNDs outline (array of 3 μND and single μND) after dip-coating μNDs in different formulations. The 3D printed μNDs have autofluorescence, which was then threshold corrected. Aqueous coating on μNDs with fluorescein dissolved in water (a), Tween-20 (b), Sucrose: (c) low (5 mg/mL w/v) and (d) high (50 mg/mL w/v), and CMC: (e) low MW and (f) high MW, all of which show partial coating as indicated by the fluorescence images. The formulations were then prepared by keeping the surfactant constant (Tween-20) while changing the viscosity enhancers, for example, coating formulation A (g) contained Tween-20, sucrose (low), and fluorescein; formulation B (h) contained Tween-20, sucrose (high) and fluorescein; formulation C (i) contained Tween-20, CMC (low), and fluorescein; formulation D (j) contained Tween-20, CMC (high), and fluorescein. The fluorescence images of coated μNDs prepared from formulations indicated that formulations A, B, and D showed uniform coating concentrated on the μND shaft only, however, since formulation B contained a high amount of sucrose, we chose not to proceed with that formulation. Formulations A and D were then used to study the effect of the number of dips (3/9/27) on the coating amount loaded. Mass of fluorescein coated on μNDs as a function of formulation and μND coated amount shown in k and l, with inset fluorescence images indicating the intensity of fluorescence proportional to the coated amount. (m) Contact angle and surface tension of water droplet and formulations A and D on a 3D printed surface (cube). Contact angle was measured on a 3D printed surface, whereas the surface tension was measured using a tensiometer. Data shown as Avg ± SD, plotted in PRISM. ****Statistical significance ($p < 0.0001$) was determined using one-way ANOVA.

theoretical models that can accurately predict the effect of surface tension and viscosity on coating uniformity and thickness, especially at the micrometer length scales of μNDs. Therefore, we dip-coated μNDs using different formulations to study their effect on coating uniformity and coating thickness.

We examined the coating dynamics of the coating formulation for dip coating of aqueous solutions (Table 1). Our first attempt to coat μNDs involved dipping in aqueous solutions containing only fluorescein as a model drug. This formulation did not produce any coating on the μND shaft (Figure 7a). The hydrodynamics of dip-coating hypothesizes that thicker coatings can be achieved by increasing the coating solution viscosity, since higher viscosity increases the hydrodynamic drag on the liquid during μND withdrawal and leads to an increase in the volume of the liquid film that is formed on the μND upon its withdrawal.[63] To that end, sucrose and CMC (viscosity enhancers) were separately tested by adding them to the aqueous coating formulations. Tween-20 (surfactant) (Figure 7b) was not included in the formulation to elucidate the effect of the viscosity enhancers. Both sucrose (low: 5% w/v, high: 50% w/v) and CMC (low MW and high MW) formulations produced a thicker but uneven coating on the μND shafts (Figure 7c–f). However, the coating was seen to be localized toward the center and away from the μND tip (Figure 7c–f). This occurrence of dewetting implied that the high surface tension of the viscosity enhancer containing aqueous formulations induced contraction of the liquid film on the μND during the drying phase. Therefore, we simultaneously modified the surface tension and the viscosity of the coating formulations by adding both the surfactant and the viscosity enhancer, which resulted in thick and uniform coatings (Figure 7g–j). Formulations containing sucrose (low and high w/v, Figure 7g,h) and CMC (high MW, Figure 7j) yielded a more uniform coating throughout the μND shaft. Thus, optimizing the macroscale principles of thermodynamics and hydrodynamics of wetting and dip-coating to the micrometer length scale of μNDs has enabled the formation

https://doi.org/10.1021/acsbiomaterials.4c00905
ACS Biomater. Sci. Eng. XXXX, XXX, XXX−XXX

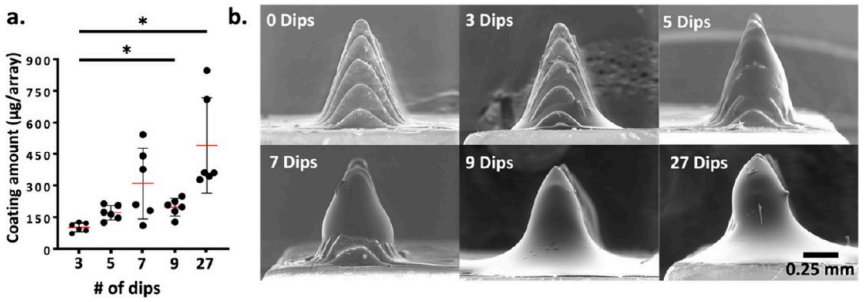

Figure 8. Effect of the number of dips on the coating efficiency of NMN drug on 3D printed µNDs. (a) Quantitative analysis of the average NMN coated amount (µg) as a function of the number of dips (n = 6, data shows Avg ± SD, plotted in PRISM; *Statistical significance [<0.1] was determined using the one-way ANOVA). (b) SEM images of coated µNDs (3/5/7/9/27 dips).

of uniform coatings on µNDs by matching the surface energies of the coating solution and the material to promote wetting and of thicker coatings by increasing the viscosity (viscosity enhancer) of the coating solution, thereby increasing the volume of the liquid film adhering to the µND upon withdrawal from the coating solution. These two criteria form a general basis for designing coating solution formulations to produce uniform coatings on µNDs. Additionally, the thermodynamics of wetting postulates that only formulations that can completely wet the substrate (i.e., have contact angles approaching zero) can produce uniform films on the substrate.[63] The static contact angle of DI water on the 3D printed methacrylate solid surface was measured to be 88.7 ± 3° (Figure 7m-iii, water droplet). This large contact angle is the result of the aqueous coating solution having a high surface tension (72.25 ± 0.094 mN/m at 25 °C; Figure S6). Adding Tween-20 and CMC to the coating formulation D, lowered the surface tension (38.06 ± 0.293 mN/m, Figure 7m-ii) thus reducing the contact angle to 66.3 ± 3° (Figure 7m-i). However, the greatest reduction in the contact angle occurred in formulation A containing sucrose and Tween-20 (54.7 ± 1.2°, Figure 7mi), which was attributed to its low surface tension (41.63 ± 1.432 mN/m, Figure 7m-ii).

Since formulations A and D produced uniform coatings on the µND shaft, they were used to quantitatively determine the amount of fluorescein coated onto the µND shaft. The fluorescein coated µND arrays were rinsed with ethanol (200 µL, 100% v/v), and the supernatant was then measured using a spectrophotometer. The fluorescence intensity was proportionate to the amount of coated fluorescein (for fluorescein calibration of absorbance vs concentration, see Figure S7). The coating was performed over 3 days to assess for interday precision (n = 3 µNDs/treatment/day). Coating formulations containing sucrose (formulation A) and CMC (formulation D) were separately examined for the amount of fluorescein coated on the µNDs. The number of coating dips increased both the mass of drug coated onto µNDs and the thickness of the coating (Figure 7k,l). However, the amount of fluorescein coating with sucrose as the viscosity enhancer showed less spread (Figure 7k, Relative standard deviation 7.1) compared to CMC (Figure 7k, Relative standard deviation 10.1), which is indicative of the accuracy of the coating process conducted over 3 days. The average amount of fluorescein coated on the µND shafts using sucrose as the viscosity enhancer was 132 ± 20.8 to 281 ± 40.3 µg compared to the average amount coated when CMC was used as the viscosity enhancer which was 118 ± 46.2 to 238 ± 84.6 µg. These results show that sucrose is a better viscosity enhancer compared to CMC not only because of the amount of fluorescein coated onto the µNDs but also the low concentration of sucrose (5% w/v) used to make the formulation compared to CMC (1% w/v). Guided by these relationships, a single coating or multiple coatings through dip-coating method or a combination can be used to coat a predetermined mass of drug onto µNDs.

4.3.3. Coating Efficiency of NMN on 3D Printed µNDs. Following the optimization of the coating solution and the fabrication of the microtanks, we then investigated the amount of NMN coated on the µNDs using formulation A (replacing fluorescein with NMN). The number of dips examined here was 3, 5, 7, 9, and 27 dips, with 5 min drying interval between dips, conducted at room temperature consecutively over 3 days to account for the precision of the dip coating.

The average amount of coated NMN on the µND shafts increased with the number of dips (Figure 8a,b). However, only 5 (185 ± 54.9 µg) and 7 (311 ± 154 µg) dips showed coatings concentrated on the µND shaft (Figure 8a). The 9 and 27 dip µNDs also achieved a larger coating amount (9 dips: 395 ± 38.5 µg and 27 dips: 491 ± 206 µg), and the drug was also coated at the bottom of the needle shaft (SEM images of coated µND, Figure 8b). While standard deviation bars are shown for the specific experiments in the graphs in Figure 8a, the average relative standard deviation (RSD) for 5 and 7 dips was relatively high (between 16 and 19%). This relatively high variation could be attributed to the manual coating process that involved careful loading and refilling of the microtanks, drying, and multiple repeats of this process. The coating of µND arrays was performed manually in a laboratory with high water loss percentage (Figure S8); therefore, improved control of temperature and humidity in the coating environment and automation of the coating process are postulated to further reduce the RSD to within acceptable limits.

To effectively pierce the stratum corneum and deliver therapeutics, the µND must possess strong mechanical properties. However, the mechanical integrity of µNDs can be compromised by the coating solution applied to their tips.[105,106] To assess the impact of this coating, mechanical failure and transdermal drug delivery tests were conducted *in vitro*. Specifically, the mechanical properties of the NMN-coated polymer µNDs were evaluated with a texture analyzer using a compression test. As illustrated in Figure S9a, the force vs displacement graph showed that uncoated µNDs exhibited a higher compressive force compared to NMN-coated µNDs (with 5 and 7 dips), indicating structural weakening due to the coating. For all µNDs tested, the force increased until the ultimate load was reached, at which point elastic deformation occurred (Figure S9b, post mechanical test). For the 5-dip

https://doi.org/10.1021/acsbiomaterials.4c00905
ACS Biomater. Sci. Eng. XXXX, XXX, XXX−XXX

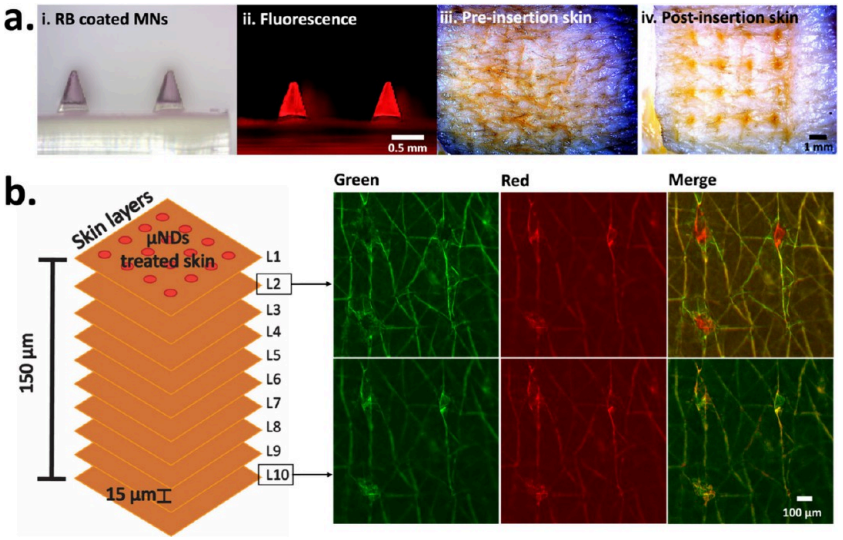

Figure 9. μND surface coating and visualization of deposition of Rose Bengal (RB) dye into the skin using coated μND array. (a) Stereomicroscopy image of a single coated needle (i) Bright field image of RB coated μNDs; RB coat is indicated as a very light red hue on the surface of the needle. (ii) Fluorescence microscopy image showing that the dye has penetrated inside the needle. (iii) Preinsertion skin and (iv) coated μND treated skin. (b) Confocal laser scanning microscopy images of the Rose Bengal (RB) μND array insertion on full thickness excised human skin. The red dots on the treated skin are representative of RB dye deposition in the skin. An illustration next to the confocal images shows the depth of imaging. The respective pseudocolored green and red channels indicate the laser excitation/emission range of 545/562 nm and 640/665 nm.

NMN-coated μNDs, buckling was observed at approximately 14.4 ± 0.59 N, followed by a significant drop in load as the μNDs continued to be compressed against a metal block after buckling. The 7-dip NMN-coated μNDs exhibited an even lower buckling load of 8.52 ± 2.64 N. In contrast, the uncoated μNDs showed a discontinuity at around 19.8 ± 1.69 N, marking the initial needle failure, after which the load continued to increase under compression. Despite the weakening effect of the coating, both the 5-dip and 7-dip NMN-coated μNDs retained fracture strengths well above the minimum force required to penetrate human skin, which is reported to be greater than 0.03 N per needle.[107] These results confirm that both 5 and 7 dip coated NMN μNDs were mechanically robust enough for practical application and thus identified for further skin studies.

4.4. Coated μND Skin Dye Visualization and NMN Permeation. *4.4.1. Dye Visualization in Skin.* To assess the insertion depth of coated μNDs into the human skin explant and visualize the distribution of drugs released from coated μNDs, 3D printed μNDs were coated with a thin uniform layer of the coating solution containing RB dye. Sucrose and Tween-20 were also added to the dye coating solution to increase adhesion and protect the integrity of the coated dye.[108] The RB dye has been shown to uniformly coat the μND shaft only (Figure 9a-i,ii), with a discontinuation of dye film seen on the base of the μND shaft (Figure 9a-ii). This confirmed the visual coating of the 3D printed μNDs. The coated μNDs were then inserted into the skin (Figure 9a-iii, skin with no μND insertion) *in vitro* and removed after 45 s application. The holes on the surface of the skin indicate microchannels created by the μNDs (Figure 9a-iv).

To examine coated RB dye diffusion into the skin, a confocal laser scanning microscope was employed to image the μND treated skin. Imaging was taken up to a depth of 150 μm into the skin, as illustrated in Figure 9b. The confocal images demonstrate the successful deposition of RB dye at 30 μm into the skin (Figure 9b, L2), whereas a disruption was visible to a maximum depth of 150 μm. The μND treated areas were clearly identifiable as circular, regular dots in the stratum corneum (SC) and all the way into viable epidermis (VE). This confirmed that the coated μNDs array not only can puncture the skin but also can deliver the coated payload into the skin.

4.4.2. In Vitro NMN Permeation Efficiency from Coated μNDs. To better understand the NMN release kinetics from the coated μNDs, NMN coated μNDs were dissolved in PBS (pH 7.4) before being analyzed in the HPLC-UV (Figure S10) and LC-MS systems (Figure S11), respectively. Both the HPLC and LC-MS data indicated clear release of NMN from the NMN coated μNDs without any degradation products.

To examine the permeation of NMN from NMN coated μNDs in human skin *in vitro*, 3, 5, and 7 dip coated NMN μNDs were applied on full thickness human skin on Franz diffusion cell setup (Figure 10a-i) with the permeation profile tracked for 24 h. First, to confirm microporation created by the μNDs, the μND treated skin was examined using SEM and histology cryosection. Micropore puncture on the skin surface due to the NMN μND arrays was characteristically showed as holes circular in shape (Figure 10a-ii). To ensure that the skin did not fold onto itself, cross-sectioning of μND treated skin tissue showed visible stratum corneum membrane disruption (Figure 10a-iii). Clear puncture sites due to NMN coated μNDs represented by the disruption of the stratum corneum and the viable epidermis were visible. This barrier breach also confirms the efficacy and the ability of these μND arrays to create microchannels in the stratum corneum, thus facilitating the passage of molecules across the skin.

For this study, only 3 dip (102.4 ± 19.5 μg), 5 dip (185 ± 54.9 μg), and 7 dip (311 ± 154 μg) coated μNDs were used. Detectable quantities of NMN were observed in the receptor chamber of Franz cells within 15 min of μND application (3 dip: 5.07 ± 0.51 μg, 5 dips: 21.5 ± 19.9 μg, and 7 dips: 30.5 ±

https://doi.org/10.1021/acsbiomaterials.4c00905
ACS Biomater. Sci. Eng. XXXX, XXX, XXX−XXX

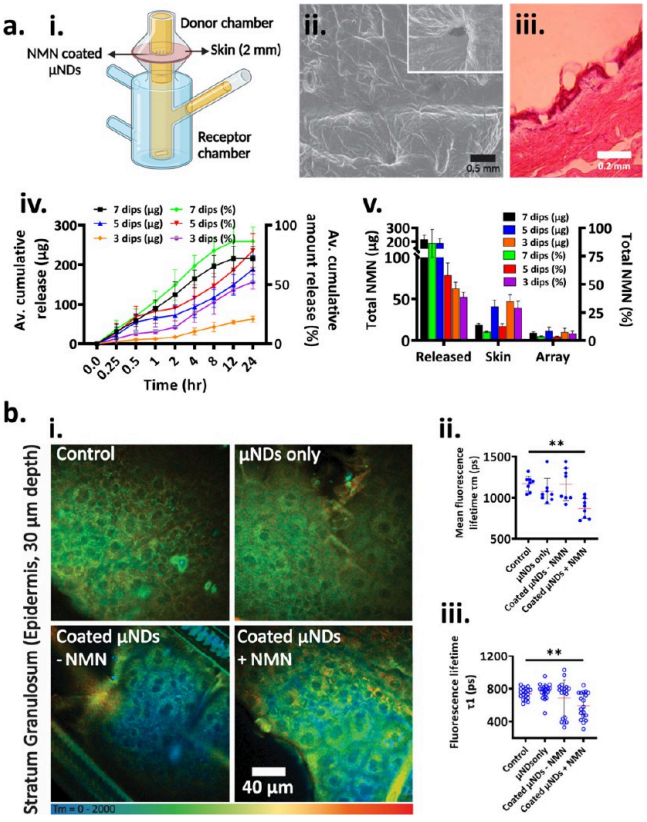

Figure 10. Illustration of skin puncture and NMN permeation profile due to NMN coated μND arrays. (a) (i) Illustration of the Franz diffusion cell setup to study the NMN diffusion kinetics in the skin. (ii) SEM image of μND treated skin with inset showing magnified image of one puncture site. (iii) Hematoxylin and eosin image of μND hole in excised human skin. The image shows a H&E stained cryosection of a μND penetration site in human skin indicated by membrane disruption. Graphical presentation of the NMN permeation profile from the NMN coated μND array (3/5/7 dip coated μNDs) treated skin showing (iv) the cumulative average NMN permeation amount (μg) and percentage (%) profiles, and (v) total NMN reconciled in this study (n = 3 μND arrays). Individual permeation amount and percentages represented as Avg ± SD. (b) NAD^+ regulation in the NMN coated μND array treated mouse ear skin *ex vivo* (n = 2) in the stratum granulosum (SG) epidermal layer. (i) Multiphoton tomography−fluorescence lifetime microscopy images of SG cells of epidermis at 30 μm in depth, control (untreated skin), μND treated skin, and coated μND ∓ NMN treated skin. Graphical presentation of subsequent (ii) mean fluorescence lifetime (τ_m) and (iii) free unbound NADH (τ_1) quantified from photons from the SG. Images are pseudocolored by offset values to distinguish cellular NAD^+ fluorescence levels (indicated by the color bar below the set of composite images, ranging from 0−2000 ps). **Statistical significance (p < 0.01) was determined using one-way ANOVA.

19.0 μg of NMN) (Figure 10a-iv). This suggests rapid dissolution of NMN from the coated layer on the μND surface upon contact with the aqueous environment in the skin interstitial fluid, thus dissolving the coated NMN. The final amount of NMN detected in the receptor chamber after 24 h was approximately 62.8 ± 7.34 μg (3 dips), 189 ± 34.5 μg (5 dips), 215 ± 30.8 μg (7 dips) of NMN. Quantitative analysis of the overall NMN used for this study (Figure 10a-v) indicated that approximately only 11.2 ± 4.52% and 3.68 ± 0.44% (5 and 7 dips) of the nominal NMN coating was recovered from the μND arrays. The tape-stripping of the μND array treated skin indicated approximately 17.1 ± 3.13% and 7.68 ± 0.55% (5 and 7 dips) of NMN remained in the skin and 78.7 ± 14.4% and 86.3 ± 12.3% (5 and 7 dips) of the nominal NMN was detected in the receptor chamber of the Franz diffusion. This study focused on quantifying the amount of NMN on skin SC using tape stripping, which was performed with 20 strips. This process only removed approximately 10 μm thickness of skin. Our aim (unlike studies on intact skin[86,87]) was to demonstrate little or no drug in the skin, as the skin barrier is breached, and moreover, our work has demonstrated there was no drug coated on the base of the μND patch (Figure 8)

4.4.3. Mechanistic Understanding of NMN Pharmacodynamics. NMN is an established precursor molecule used in the NAD^+ synthesis pathway;[74,109,110] therefore we hypothesized that delivering NMN into the skin epidermis would increase the amount of NAD^+ synthesis. For this study, only 5× dipped NMN coated μND arrays were applied onto mouse ear *ex vivo* skin samples. The skin samples were then imaged using multiphoton tomography (MPT), quantitatively assessing NAD^+ fluorescence lifetimes (τ_m) and those of free unbound NADH (τ_1).

The fluorescence of the stratum granulosum (SG) cells' endogenous fluorophores allows visualization of the detailed morphological cellular structure as well as changes caused by an external stimulant (in this case NMN) noninvasively using MPT.[90] All fluorophores have a second characteristic to distinguish them from other fluorophores, their fluorescence lifetimes (τ_m). The photon counts over time for NAD(P)H of the SG layer can in turn be used to define the fluorescence decay curve, mean τ_m, and α_1/α_2. These parameters are important to assess cellular metabolic function in a noninvasive manner. We found a significant (p = 0.0076) increase in the NADH mean τ_m in NMN coated μND treated skin (Figure 10b-i Coated μND + NMN; Figure 10b-ii, 867 ± 113 ps) compared to control skin (Figure 10b-i Control; Figure 10b-ii, 1172 ± 85.1 ps). The ratio of the coefficient amplitudes for free and bound NAD(P)H α_1/α_2, however, did not change (data not shown), although the τ_1 (free unbound NADH lifetime in picosecond) reduced to 594 ± 154 ps for Coated μND + NMN treated skin (Figure 10b-ii) compared to both untreated skin (control, 742 ± 65.1 ps, Figure 10b-ii) and Coated μND − NMN treated skin (768 ± 90.1 ps, Figure 10b-ii). This suggests that the reduced lifetime of free unbound NADH in the epidermal keratinocytes of mice ear skin is due to the NMN released from the NMN coated μND arrays.

5. DISCUSSION

The surface resolution of μND arrays made in this study compares favorably to previously developed μND arrays fabricated using low-cost DLP (vat photopolymerization)-based AM methods reported in the literature.[29,34,54] The two main advantages of the DLP-based AM method over the Fused Deposition Modeling (FDM) based AM method are significant improvement in the printing resolution within the micrometer range and in the single fabrication step, rendering a smoother surface compared to the two-step fabrication method (FDM).[29] Despite those advantages, replicating superior dimensional resolution using low-cost SLA 3D printers in the past has shown variable results,[38,43−47] since most 3D printed μNDs were fabricated using highly expensive 3D printers.[34,54] In this study, a significantly lower-cost benchtop vat photopolymerization 3D printer (Phrozen, Taiwan) with higher printing resolution (40 μm spot size) was used to

https://doi.org/10.1021/acsbiomaterials.4c00905
ACS Biomater. Sci. Eng. XXXX, XXX, XXX−XXX

produce μNDs with increased surface resolution, thus improving the 3D design input to output ratio. This was achieved by a combination of modifying the original 3D printer resin and optimizing other key printing parameters. By controlling key design parameters, such as print layer (controlled by the movement of the build plate), print angle (spatially rotating the model in CAD design), and aspect ratio (height/base diameter ratio), this study demonstrated quick and facile production of high-resolution μND arrays.

The first design parameter investigated in the parametric study was the effect of the layer height on the μND quality. The Phrozen 3D printer was able to print needles of acceptable quality using 15, 25, 50, and 100 μm layer height. Decreasing the print layer height resulted in a markedly improved and smoother surface finish as the edges of the μND surface at an angle to the *z*-axis became smoother. Edge ridge mismatches are a consequence of the stair-stepping phenomenon that is inherent to printing in layers but become less pronounced with decreasing layer height.[52] At 100 μm layer height, the structural integrity was compromised by the relatively large layer height which resulted in more pronounced edge ridge mismatches thus increasing local stress concentrations (Figure 3c-i). Increasing the layer height print setting involves shorter print time and decreased risk of print failure due to a smaller number of individual layers to be cured. As the μNDs printed in this study were in the micrometer range, consisting of a relatively low number of layers, even with a 25 μm layer height print setting, both of these advantages were negligible. We therefore decided to continue with the parametric study using a 25 μm layer height, which resulted in a smooth needle surface finish. Despite the smoother surface of the μNDs, the output needle height was still lower than the input value (Figure 3c-ii). Therefore, we sought to improve that parameter by optimizing the print angle. In general, μND arrays are designed using a CAD program and then 3D printed, where the backing layer and the base of μNDs are produced in a similar manner to the input design due to the curing of a sufficiently wide single stacking layer (at 0° print angle). The limitation here is that the single stacking area becomes narrower (reaching the μND tip) producing inaccurate and inconsistent printing of tip shape. In our study, the stacking area, including the tip, was widened by adjusting the print angle. In doing so, the stacking area, including the μND tip, increased as the stacking direction of the object was spatially changed during the CAD design (Figure 4a-i). This study demonstrated improved input to output height % and tip diameter as the print angle approached 90°, yielding high output μNDs (Figure 4a-ii). Despite this, the output needle height was still lower than the input value; therefore, we sought to improve that by optimizing the print aspect ratio. The aspect ratio of a μND is defined as the ratio of the μND height to base diameter, and this value is generally lower for a real μND with respect to that of a perfect μND (i.e., a needle of infinite tip sharpness) due to its inherently decreased base diameter resulting from tip rounding. Our study demonstrated that increasing base diameter was relatively proportionate to the input value for μNDs of greater output height (Figure 4b-i). As the needle input base diameter decreased below a value of about 400 μm, we observed a greater increase of the height discrepancy, resulting in μNDs with high aspect ratios. This can be seen in Figure 4b-i and Figure 5a, where the smaller base diameter μNDs appear asymmetrical, unlike their input shape. This limitation is most likely related to the minimum feature size in the *x*−*y* print plane and the realistic laser spot size, even though the 3D printer manufacturer claims a 40 μm spot size. Nonetheless, the output μND height was closer to the input value (86−90%), and the tip diameter was smaller (<40 μm) at a lower aspect ratio of 1:1.7 (Figure 4b-iii). To further improve the 3D print input to output height %, we examined whether increasing the print curing time would improve the μND output height. The output height of the 3D printed μNDs showed a trend of increasing tip radius with decreasing needle height (Figure 5a). While the printed μNDs were shorter than specified in the input model, this appeared to be a predictable factor.

This difference between input and output dimensions is attributed to the tessellation effect by the software which converts the CAD design model to a printable model, the minimum UV dose supplied during the photopolymerization process, and the way a layer is drawn.[34,52] UV light is diffractive, and instead of focusing on a single spot, it will smear out into a blurred spot at the image plane.[34,52] A layer is typically cured by a laser tracing the outline of the "cross-sectional slice" and "cross-hatching" the space between.[34,52] The gap between the laser traces while hatching is known as hatch spacing and that controls the overlap.[34,52] The closer the hatch spacing, the more overlap exists, and that consequently yields a more complete cure.[34,52] With conical μND design, the decreasing size of the cross-sectional slice (relative to the center of the slice) results in reduction in overlapping occurrence, and therefore an overall lesser UV dose for a given point, i.e., areas closer to the center of the slice would be affected less compared to areas further away by not receiving the critical UV dose required for the polymerization process. This process continues gradually as the cross-sectional area further decreases as it reaches round shaped μND tips before reaching full needle input height.[34,52] This also explains the increased input-to-output height discrepancy for higher aspect ratio μNDs compared to that for lower aspect ratio ones, due to a lower cross-sectional surface area in the *x*−*y* plane, as seen in Figure 4b. Regardless, the tip diameter in this study is among the sharpest needles printed using a low-cost 3D printer to date.

The successful delivery of therapeutics through coated μNDs depends on the reliability and uniformity of coating a controlled drug film on the μND surfaces. Another important component of the micro-dip-coating process is the dip-coating device itself. Simply dipping μNDs into a large container containing coating formulation has resulted in contamination of the μND base (Figure 6a-vii). Capillary forces are mainly responsible for the rise of the free meniscus along the μND shaft, eventually pulling the formulation to touch the μND base. This effect is amplified in an array due to the close spacing of the μNDs, which enhances the capillary effect and can lead to bridging of the coating solution between adjacent μNDs, as demonstrated in our study. To address these issues, we have developed a 3D printed dip-coating microtank design that uses dip holes with dimensions similar to that of individual μNDs instead of a large space, thus preventing the meniscus rise and physically masking the base substrate between μNDs, as individual needles are now independent determinants of microsurface phenomena (Figure 6b-iv). Using this micro-dip-coating device, coating deposition can be highly controlled to localize only on the μND shaft and, when desirable, in a reproducible manner (Figure 6a). Concerning the practicality of the microtank dip coating device developed in our study, it

https://doi.org/10.1021/acsbiomaterials.4c00905
ACS Biomater. Sci. Eng. XXXX, XXX, XXX−XXX

only required very small volumes of coating solution (Figure 8c), ranging from 4 μL/well for 3 dip to 36 μL for 27 dip out-of-plane arrays. This is important since many experimental and established biotherapeutics are expensive and available only in limited quantity. Prausnitz et al. also identified the formation of air bubbles, which can interfere in the coating process, therefore rendering the coating process less effective.[63] To alleviate this, holes were added into the back of the array to prevent the formation of air pockets (Figure 6b-i).

Using the new microtank coating device, our initial attempts to coat μNDs by dipping into an aqueous drug solution containing fluorescein resulted in zero coating surface coverage on the μND shaft (Figure 7a). Our first approach to solve this problem was modifying the coating formulation by increasing the viscosity and reducing the surface tension using 5% (w/v) sucrose and 0.01% (w/v) Tween-20 as the viscosity enhancer and surfactant, respectively. This enabled complete and uniform coverage of the dipped μND surface (Figure 7g). This coating formulation has been shown to be very versatile in our study. The two excipients used to modify the coating formulation are FDA approved excipients used in injectable formulations; therefore, this coating formulation should also be safe for use in humans.

The administration of the nicotinamide mononucleotide (NMN) to increase plasma NAD^+ levels has been shown to ameliorate age-associated pathophysiologies and disease conditions, such as restoring NAD^+ biosynthesis in impaired pancreatic beta cells[69] and improvement of metabolic disorders such as obesity and diabetes through NAD^+ mediated pathways.[70−74] However, due to first pass metabolism, an increased amount of NMN is currently orally delivered.[110−113] Therefore, the objective of this study was to deliver NMN transdermally by using coated μNDs as a potential alternative to oral delivery. Our coated μNDs were capable of penetrating the skin of up to 150 μm deep into the dermis layer of the skin tissue (Figure 9b), even though the μND height was approximately 800 μm. This notable difference is due to the skins' resistive force acting against the μND insertion,[2] since the elastin fibers and collagen within the dermal layer provide strength and flexibility, with increasing stiffness as the fibers straighten.[2,114,115] This, however, had minimal effect when delivering a model dye molecule (Rose Bengal) deep into human donor skin *in vitro*, as evident by the μND coated Rose Bengal dye fluorescence signal detected as deep as 100 μm in the skin (Figure 9b), and NMN permeation through full thickness skin (Figure 10a-iv). It is important to note, however, that two different insertion methods were employed for skin insertion studies: thumb force for initial application and a texture analyzer for assessing skin membrane disruption, each serving specific purposes. Thumb force was used to simulate real-world patient application, ensuring practical relevance, while the texture analyzer provided a controlled and consistent force of 20 N to ensure reproducibility in assessing micropore creation. The texture analyzer data establishes a benchmark for optimal insertion force, addressing concerns about translational reproducibility and informing the design of patient instructions or applicator devices. Although both methods have produced micropuncture sites on the skin, it is noteworthy that a force beyond 20 N is sufficient to effectively pierce the skin in these experiments.

NMN permeation from the coated μND arrays in the skin included two stages: the dissolution of the coated NMN in the skin and the diffusion/permeation of NMN in the skin. The dissolution of the coated NMN from the μND arrays was quick soon after insertion, as evident by the NMN detection in the receptor chamber within 30 min postapplication, followed by a gradual release over 24 h of approximately 250 μg of NMN (Figure 10a-iv). A past study demonstrated significant pharmacodynamic effect when NMN plasma levels were above 40 μM within 14 h after intraperitoneal (ip) administration of NMN (500 mg/kg body weight) in female mice.[71] Assuming that the biodistribution route of drug released from μND arrays is similar to the ip rather than the oral route, to achieve NMN plasma levels of 40 μM, we would require an NMN amount equivalent to 12.6 mg (40 μM × 314.219 μg/μmol). By this rationale, NMN μND arrays containing a NMN nominal load of approximately 1695 μg of NMN (approximately 6 arrays with 16 μNDs each) could potentially deliver therapeutically relevant doses of NMN in mice studies *in vivo*.

The μND patches in our study were engineered for single-use applications, aligning with standard practices in drug delivery systems to guarantee both efficacy and safety. By limiting μNDs to a single use, we eliminate any potential impacts on subsequent applications that could arise from the drug loading method. While surface coating techniques, especially those utilizing viscosity enhancers and surfactants, can influence drug loading capacity and release profiles, these effects are primarily relevant during the first application. Our findings demonstrated 78.7 ± 14.4% and 86.3 ± 12.3% of the nominal NMN amount (5 dip: 185 ± 54.9 μg and 7 dip: 311 ± 154 μg) successfully dissolved from the μND tips and diffused through full-thickness human skin *in vitro* (Figure 10). For single-use applications, the critical factors are the uniformity and reproducibility of the drug loading across each patch. Research consistently shows that single-use μND patches deliver precise medication doses, minimizing variability risks associated with repeated use.[66,67,117] Consequently, the drug loading method's influence is effectively confined to the initial intended use of each patch, ensuring reliable and consistent therapeutic outcomes. In addition, our results indicate a faster and higher release/permeation with the 7× dip coated μNDs compared to the 5× and 3× coatings that can be attributed primarily to the increased dose rather than just the coating thickness (Figure 10a). While a thicker coating might suggest a longer dissolution time, it also results in a greater quantity of the active ingredient available for release, creating a steeper concentration gradient and thereby enhancing permeation. The dissolution time may not linearly correlate with coating thickness if dissolution is diffusion-controlled and the surface area exposed to the receptor medium remains consistent across different dipping cycles.[118,119] Therefore, the higher dose provided by the 7× coating significantly impacts the overall release and permeation profile. This highlights the importance of optimizing coating thickness not only for dissolution kinetics but also for controlling dose-dependent permeation characteristics of the μND system.

Currently invasive/destructive methods such as immunohistochemistry, metabolic assays, and PCR used to measure cell metabolism both *in vitro* and in tissues are used to determine NAD^+ regulation in cells. These techniques are laborious and invasive, which often render cells unviable and unrecoverable for *in vivo* dynamic observations. We also report a noninvasive optical technique to interrogate the upregulation of NAD^+ in keratinocytes (*ex vivo*) when treated with NMN coated μND arrays. This technique exploits intrinsic autofluorescence of

https://doi.org/10.1021/acsbiomaterials.4c00905
ACS Biomater. Sci. Eng. XXXX, XXX, XXX−XXX

cells and tissues using multiphoton microscopy. We demonstrate that fluorescence of the endogenous NADH in the HaCaT cells show a decreasing trend in both the average fluorescence lifetime (τ_m) and the free unbound NADH (τ_1), while we see an increasing trend in the NADH/NAD^+ cellular redox ratio, with increasing dosage of NMN administration. Haridass et al. have previously demonstrated a similar trend and concluded it was indicative of cell death due to cellular metabolic stress after the application of their Nanopatch.[116] This was, however, not the case in our study, since our data showed a difference in both the fluorescence lifetimes τ_m and free unbound NADH τ_1 between the skin treated with NMN μND arrays and the skin treated with μND arrays without NMN (Figure 10b-ii,iii). This confirms that the reduced τ_m and τ_1 is caused by the NMN embedded in the μND rather than the mechanical stress exerted by the microprojections on keratinocytes. This pharmacodynamic effect elicited by NMN coated μND arrays demonstrates a viable and alternative route of drug administration through the dermal route.

The application of 3D printing in the fabrication of solid μNDs is a relatively simple method that can be adapted by researchers with only basic skills in CAD design required. Our proposed optimization method offers a viable alternative to manufacturing highly resolved μND arrays, including the ability to design and fabricate multiple μND array designs in a short time (approximately 2 h/30 arrays) at a relatively low cost. Additionally, as benchtop 3D printers are suitable for use in the lab, molds can be fabricated in-lab without requiring expensive machining instruments.

While the AM method generally allows for fabrication of more complex geometries which is not possible with conventional subtractive manufacturing methods, our study chose to manufacture conical-shaped straight μNDs as our choice of design for several reasons. Conical-shaped needles are extensively used in μND research and the most common and preferred design, therefore offering a simple low-cost manufacturing method that greatly benefits the researcher. Lastly, the resolution of the Phrozen printer could pose a limit on more complex μND structures, although recent advances in light technology have resulted in improved 3D printer performance by reducing the spot size to 20 μm. Desktop 3D printers (Phrozen 4K and 8K) are becoming rapidly abundant in the research environment since they allow for rapid prototyping. Therefore, such printers may already be available to laboratories focusing on μND research, aiding in the adaptation of this fabrication technique. The methods outlined here could also facilitate the optimization of direct fabrication of μND arrays made from biocompatible photocurable polymers, which are becoming more readily available.

6. CONCLUSION

This study developed a very low-cost, simple, and customizable method for the fabrication of μND arrays by means of a commonly used, commercially available, and affordable 3D printer. The resin viscosity was modified to help with the manufacturing of μNDs with enhanced micrometer surface topography. A parametric study showed that printing μNDs with excellent tip sharpness beyond the 3D printer's defined resolution limits is possible with correct print settings. Printed μND parameters showed a discrepancy from those in the virtual CAD model. Compared with the model, the printed needles were found to be shorter and have a greater than specified aspect ratio, but this was corrected by controlling the print layer height, print angle, and aspect ratio.

To our knowledge, this is the first study where an innovative micro-dip-coating device was designed and fabricated on demand with a low-cost benchtop 3D printer to control surface tension driven wicking of coating solution up μND shafts. The coating formulation was also developed to achieve uniform coating and spread on μNDs by using low concentrations of the viscosity enhancer sucrose and reducing the surface tension by adding the surfactant Tween-20 as coating excipients. Taking these findings into consideration, μND arrays were coated for the first time with a NAD^+ precursor small molecule, NMN, with increased accuracy and without contaminating the μND base. The coated 3D printed μND array was able to deliver the nutraceutical molecule NMN into human skin, as well as regulate the NAD^+ levels in the mouse ear model. The fabrication method demonstrated here can be directly applied by μND researchers in-lab regardless of microfabrication expertise or access to workshops with specialized instruments, while allowing rapid prototyping of μND arrays with parameters tailored toward their specific requirements.

■ ASSOCIATED CONTENT

Supporting Information

The Supporting Information is available free of charge at https://pubs.acs.org/doi/10.1021/acsbiomaterials.4c00905.

Specifications of various 3D printers in the literature, set up for contact angle measurement, viscosity changes and FTIR of original and modified resin, effect of print angle on μND height, cell viability on 3D printed discs, drop coating technique, surface tension of formulations, calibration curves for fluorescein formulations, evaporation rates of formulations, mechanical tests of μND arrays, pharmaceutical analysis of NMN from coated μNDs (PDF)

■ AUTHOR INFORMATION

Corresponding Authors

Tushar Kumeria − *School of Materials Science and Engineering and Australian Centre for Nanomedicine, The University of New South Wales, Sydney, NSW 2052, Australia;* orcid.org/0000-0003-3351-7148; Email: t.kumeria@unsw.edu.au

Yousuf Mohammed − *Frazer Institute, Faculty of Medicine and School of Pharmacy, The University of Queensland, Brisbane, QLD 4102, Australia;* orcid.org/0000-0002-7825-7557; Email: y.mohammed@uq.edu.au

Authors

Masood Ali − *Frazer Institute, Faculty of Medicine, The University of Queensland, Brisbane, QLD 4102, Australia;* orcid.org/0000-0002-8783-845X

Sarika Namjoshi − *Frazer Institute, Faculty of Medicine, The University of Queensland, Brisbane, QLD 4102, Australia*

Khanh Phan − *School of Agriculture and Food Sciences, The University of Queensland, Brisbane, QLD 4072, Australia*

Xiaoxin Wu − *Centre for Biomedical Technologies, School of Mechanical, Medical and Process Engineering, Queensland University of Technology, Brisbane, QLD 4059, Australia*

Indira Prasadam − *Centre for Biomedical Technologies, School of Mechanical, Medical and Process Engineering, Queensland University of Technology, Brisbane, QLD 4059, Australia*
Heather A. E. Benson − *Curtin Medical School, Curtin University, Bentley, WA 6102, Australia*

Complete contact information is available at: https://pubs.acs.org/10.1021/acsbiomaterials.4c00905

Author Contributions

Masood Ali conceptualized the idea, wrote the original manuscript draft, conducted the experiments, analyzed data, developed methodology, and edited the manuscript. Khanh Phan performed investigation and formal analysis. Xiaoxin Wu, Indira Prasadam, Sarika Namjoshi, and Heather Benson edited the manuscript. Tushar Kumeria and Yousuf Mohammed conceptualized the idea, supervised and oversaw experiments, developed methodology, analyzed data, and provided support with manuscript editing and resources, submission, and management of the article.

Notes

The authors declare no competing financial interest.

■ ACKNOWLEDGMENTS

This work was based on a part of Masood Ali's Ph.D. thesis. The authors would like to express their appreciation and acknowledge the mouse ear skin (cadaver) donated by Dr. Ran Wang (Mater research Institute- UQ), from which the *ex vivo* imaging was possible. The authors acknowledge the facilities and the scientific and technical assistance of the Microscopy Australia Facility at the Centre for Microscopy and Microanalysis (CMM), The University of Queensland (UQ), and Dr. Cameron Flegg at the Translational Research Institute (TRI) Microscopy core facility for his help with the imaging of skin.

■ REFERENCES

(1) Gill, H. S.; Denson, D. D.; Burris, B. A.; Prausnitz, M. R. Effect of Microneedle Design on Pain in Human Volunteers. *Clinical Journal of Pain* **2008**, *24* (7), 585−594.
(2) Ali, M.; Namjoshi, S.; Benson, H. A. E.; Kumeria, T.; Mohammed, Y. Skin biomechanics: Breaking the dermal barriers with microneedles. *Nano TransMed.* **2022**, *1* (1), No. 9130002.
(3) Ali, M.; Namjoshi, S.; Benson, H. A. E.; Mohammed, Y.; Kumeria, T. Dissolvable polymer microneedles for drug delivery and diagnostics. *J. Controlled Release* **2022**, *347*, 561−589.
(4) Mohammed, Y. H.; Yamada, M.; Lin, L. L.; Grice, J. E.; Roberts, M. S.; Raphael, A. P.; Benson, H. A. E.; Prow, T. W. Microneedle Enhanced Delivery of Cosmeceutically Relevant Peptides in Human Skin. *PLoS One* **2014**, *9* (7), No. e101956.
(5) Johnson, A. R.; Caudill, C. L.; Tumbleston, J. R.; Bloomquist, C. J.; Moga, K. A.; Ermoshkin, A.; Shirvanyants, D.; Mecham, S. J.; Luft, J. C.; DeSimone, J. M. Single-step fabrication of computationally designed microneedles by continuous liquid interface production. *PloS one* **2016**, *11* (9), No. e0162518.
(6) Arora, A.; Prausnitz, M. R.; Mitragotri, S. Micro-scale devices for transdermal drug delivery. *Int. J. Pharmaceut* **2008**, *364* (2), 227−236.
(7) Kim, M.; Yang, H.; Kim, S.; Lee, C.; Jung, H. The Troy Microneedle: A Rapidly Separating, Dissolving Microneedle Formed by Cyclic Contact and Drying on the Pillar (CCDP). *PLoS One* **2015**, *10* (8), No. e0136513.
(8) Yang, H.; Kim, S.; Huh, I.; Kim, S.; Lahiji, S. F.; Kim, M.; Jung, H. Rapid implantation of dissolving microneedles on an electrospun pillar array. *Biomaterials* **2015**, *64*, 70−77.
(9) Chang, H.; Chew, S. W. T.; Zheng, M.; Lio, D. C. S.; Wiraja, C.; Mei, Y.; Ning, X.; Cui, M.; Than, A.; Shi, P.; et al. Cryomicroneedles for transdermal cell delivery. *Nature Biomedical Engineering* **2021**, *5* (9), 1008−1018.
(10) Römgens, A. M.; Bader, D. L.; Bouwstra, J. A.; Baaijens, F. P. T.; Oomens, C. W. J. Monitoring the penetration process of single microneedles with varying tip diameters. *J. Mech Behav Biomed Mater.* **2014**, *40*, 397−405.
(11) Han, D.; Morde, R. S.; Mariani, S.; La Mattina, A. A.; Vignali, E.; Yang, C.; Barillaro, G.; Lee, H. 4D Printing of a Bioinspired Microneedle Array with Backward-Facing Barbs for Enhanced Tissue Adhesion. *Adv. Funct. Mater.* **2020**, *30* (11), No. 1909197.
(12) Tran, L.; Nguyen, T.; Park, W. Bio-Inspired Barbed Microneedle for Skin Adhesion with Interlocking Mechanics. In *2019 IEEE 32nd International Conference on Micro Electro Mechanical Systems (MEMS)*, 27−31 Jan. 2019, IEEE, 2019; pp 547−550. DOI: .
(13) Liu, S.; Chu, S.; Banis, G. E.; Beardslee, L. A.; Ghodssi, R. Biomimetic Barbed Microneedles for Highly Robust Tissue Anchoring. In *2020 IEEE 33rd International Conference on Micro Electro Mechanical Systems (MEMS)*, 18−22 Jan. 2020, IEEE, 2020; pp 885−888. DOI: .
(14) Kolluru, C.; Gupta, R.; Jiang, Q.; Williams, M.; Gholami Derami, H.; Cao, S.; Noel, R. K.; Singamaneni, S.; Prausnitz, M. R. Plasmonic Paper Microneedle Patch for On-Patch Detection of Molecules in Dermal Interstitial Fluid. *ACS Sens* **2019**, *4* (6), 1569−1576.
(15) Samant, P. P.; Prausnitz, M. R. Mechanisms of sampling interstitial fluid from skin using a microneedle patch. *P Natl. Acad. Sci. USA* **2018**, *115* (18), 4583−4588.
(16) Chang, H.; Zheng, M.; Yu, X.; Than, A.; Seeni, R. Z.; Kang, R.; Tian, J.; Khanh, D. P.; Liu, L.; Chen, P.; et al. A Swellable Microneedle Patch to Rapidly Extract Skin Interstitial Fluid for Timely Metabolic Analysis. *Adv. Mater.* **2017**, *29* (37), No. 1702243.
(17) Than, A.; Liu, C.; Chang, H.; Duong, P. K.; Cheung, C. M. G.; Xu, C.; Wang, X.; Chen, P. Self-implantable double-layered micro-drug-reservoirs for efficient and controlled ocular drug delivery. *Nat. Commun.* **2018**, *9* (1), 4433.
(18) Migdadi, E. M.; Courtenay, A. J.; Tekko, I. A.; McCrudden, M. T. C.; Kearney, M. C.; McAlister, E.; McCarthy, H. O.; Donnelly, R. F. Hydrogel-forming microneedles enhance transdermal delivery of metformin hydrochloride. *J. Controlled Release* **2018**, *285*, 142−151.
(19) Ruggiero, F.; Vecchione, R.; Bhowmick, S.; Coppola, G.; Coppola, S.; Esposito, E.; Lettera, V.; Ferraro, P.; Netti, P. Electro-drawn polymer microneedle arrays with controlled shape and dimension. *Sens. Actuators, B* **2018**, *255*, 1553−1560.
(20) Chen, Z.; Ye, R.; Yang, J.; Lin, Y.; Lee, W.; Li, J.; Ren, L.; Liu, B.; Jiang, L. Rapidly Fabricated Microneedle Arrays Using Magneto-rheological Drawing Lithography for Transdermal Drug Delivery. *ACS Biomaterials Science & Engineering* **2019**, *5* (10), 5506−5513.
(21) Chiaranairungroj, M.; Pimpin, A.; Srituravanich, W. Fabrication of high-density microneedle masters towards the commercialisation of dissolving microneedles. *Micro & Nano Letters* **2018**, *13* (3), 284−288.
(22) Trautmann, A.; Roth, G.-L.; Nujiqi, B.; Walther, T.; Hellmann, R. Towards a versatile point-of-care system combining femtosecond laser generated microfluidic channels and direct laser written microneedle arrays. *Microsystems & Nanoengineering* **2019**, *5* (1), 6.
(23) Celis, P.; Vazquez, E.; Soria-Hernández, C. G.; Bargnani, D.; Rodriguez, C. A.; Ceretti, E.; García-López, E. Evaluation of Ball End Micromilling for Ti6Al4V ELI Microneedles Using a Nanoadditive Under MQL Condition. *International Journal of Precision Engineering and Manufacturing-Green Technology* **2022**, *9* (5), 1231−1246.
(24) García-López, E.; Siller, H. R.; Rodríguez, C. A. Study of the fabrication of AISI 316L microneedle arrays. *Procedia Manufacturing* **2018**, *26*, 117−124.
(25) Li, Y.; Aoude, H. Blast response of beams built with high-strength concrete and high-strength ASTM A1035 bar. *International Journal of Impact Engineering* **2019**, *130*, 41−67.
(26) Chen, Z.; Ren, L.; Li, J.; Yao, L.; Chen, Y.; Liu, B.; Jiang, L. Rapid fabrication of microneedles using magnetorheological drawing lithography. *Acta Biomaterialia* **2018**, *65*, 283−291.

(27) Sood, A. K.; Ohdar, R. K.; Mahapatra, S. S. Parametric appraisal of mechanical property of fused deposition modelling processed parts. *Materials & Design* **2010**, *31* (1), 287−295.
(28) Chohan, J. S.; Singh, R.; Boparai, K. S.; Penna, R.; Fraternali, F. Dimensional accuracy analysis of coupled fused deposition modeling and vapour smoothing operations for biomedical applications. *Compos Part B-Eng.* **2017**, *117*, 138−149.
(29) Luzuriaga, M. A.; Berry, D. R.; Reagan, J. C.; Smaldone, R. A.; Gassensmith, J. J. Biodegradable 3D printed polymer microneedles for transdermal drug delivery. *Lab Chip* **2018**, *18* (8), 1223−1230.
(30) Tang, T. O.; Holmes, S.; Dean, K.; Simon, G. P. Design and fabrication of transdermal drug delivery patch with milliprojections using material extrusion 3D printing. *J. Appl. Polym. Sci.* **2020**, *137* (23), No. 48777.
(31) Kavaldzhiev, M.; Perez, J. E.; Ivanov, Y.; Bertoncini, A.; Liberale, C.; Kosel, J. Biocompatible 3D printed magnetic micro needles. *Biomedical Physics & Engineering Express* **2017**, *3* (2), No. 025005.
(32) Faraji Rad, Z.; Nordon, R. E.; Anthony, C. J.; Bilston, L.; Prewett, P. D.; Arns, J.-Y.; Arns, C. H.; Zhang, L.; Davies, G. J. High-fidelity replication of thermoplastic microneedles with open microfluidic channels. *Microsystems & nanoengineering* **2017**, *3* (1), 17034.
(33) Caudill, C. L.; Perry, J. L.; Tian, S.; Luft, J. C.; DeSimone, J. M. Spatially controlled coating of continuous liquid interface production microneedles for transdermal protein delivery. *J. Controlled Release* **2018**, *284*, 122−132.
(34) Krieger, K. J.; Bertollo, N.; Dangol, M.; Sheridan, J. T.; Lowery, M. M.; O'Cearbhaill, E. D. Simple and customizable method for fabrication of high-aspect ratio microneedle molds using low-cost 3D printing. *Microsystems & Nanoengineering* **2019**, *5* (1), 42.
(35) Jeong, J.; Park, J.; Lee, S. 3D printing fabrication process for fine control of microneedle shape. *Micro and Nano Systems Letters* **2023**, *11* (1), 1.
(36) Xu, X.; Seijo-Rabina, A.; Awad, A.; Rial, C.; Gaisford, S.; Basit, A. W.; Goyanes, A. Smartphone-enabled 3D printing of medicines. *Int. J. Pharm.* **2021**, *609*, No. 121199.
(37) Vinayakumar, K. B.; Silva, M. D.; Martins, A.; Mundy, S.; González-Losada, P.; Sillankorva, S. Levofloxacin-Loaded Microneedles Produced Using 3D-Printed Molds for Klebsiella Pneumoniae Biofilm Control. *Advanced Therapeutics* **2023**, *6* (6), No. 2200320.
(38) Baykara, D.; Bedir, T.; Ilhan, E.; Mutlu, M. E.; Gunduz, O.; Narayan, R.; Ustundag, C. B. Fabrication and optimization of 3D printed gelatin methacryloyl microneedle arrays based on vat photopolymerization. *Front Bioeng Biotechnol* **2023**, *11*, No. 1157541.
(39) Lim, S. H.; Ng, J. Y.; Kang, L. Three-dimensional printing of a microneedle array on personalized curved surfaces for dual-pronged treatment of trigger finger. *Biofabrication* **2017**, *9* (1), No. 015010.
(40) Economidou, S. N.; Pere, C. P. P.; Reid, A.; Uddin, M. J.; Windmill, J. F. C.; Lamprou, D. A.; Douroumis, D. 3D printed microneedle patches using stereolithography (SLA) for intradermal insulin delivery. *Mater. Sci. Eng. C Mater. Biol. Appl.* **2019**, *102*, 743−755.
(41) Uddin, M. J.; Scoutaris, N.; Economidou, S. N.; Giraud, C.; Chowdhry, B. Z.; Donnelly, R. F.; Douroumis, D. 3D printed microneedles for anticancer therapy of skin tumours. *Materials Science and Engineering: C* **2020**, *107*, No. 110248.
(42) Economidou, S. N.; Pissinato Pere, C. P.; Okereke, M.; Douroumis, D. Optimisation of Design and Manufacturing Parameters of 3D Printed Solid Microneedles for Improved Strength, Sharpness, and Drug Delivery. *Micromachines (Basel)* **2021**, *12* (2), 117.
(43) Xenikakis, I.; Tsongas, K.; Tzimtzimis, E. K.; Zacharis, C. K.; Theodoroula, N.; Kalogianni, E. P.; Demiri, E.; Vizirianakis, I. S.; Tzetzis, D.; Fatouros, D. G. Fabrication of hollow microneedles using liquid crystal display (LCD) vat polymerization 3D printing technology for transdermal macromolecular delivery. *Int. J. Pharm.* **2021**, *597*, No. 120303.
(44) Monou, P. K.; Andriotis, E. G.; Tsongas, K.; Tzimtzimis, E. K.; Katsamenis, O. L.; Tzetzis, D.; Anastasiadou, P.; Ritzoulis, C.; Vizirianakis, I. S.; Andreadis, D.; et al. Fabrication of 3D Printed Hollow Microneedles by Digital Light Processing for the Buccal Delivery of Actives. *ACS Biomaterials Science & Engineering* **2023**, *9* (8), 5072−5083.
(45) Razzaghi, M.; Akbari, M. The Effect of 3D Printing Tilt Angle on the Penetration of 3D-Printed Microneedle Arrays. *Micromachines (Basel)* **2023**, *14* (6), 1157.
(46) Erkus, H.; Bedir, T.; Kaya, E.; Tinaz, G. B.; Gunduz, O.; Chifiriuc, M.-C.; Ustundag, C. B. Innovative transdermal drug delivery system based on amoxicillin-loaded gelatin methacryloyl microneedles obtained by 3D printing. *Materialia* **2023**, *27*, No. 101700.
(47) Chen, Z.; Wu, H.; Zhao, S.; Chen, X.; Wei, T.; Peng, H.; Chen, Z. 3D-Printed Integrated Ultrasonic Microneedle Array for Rapid Transdermal Drug Delivery. *Mol. Pharmaceutics* **2022**, *19* (9), 3314−3322.
(48) Razzaghi, M.; Akbari, M. The Effect of 3D Printing Tilt Angle on the Penetration of 3D-Printed Microneedle Arrays. *Micromachines* **2023**, *14* (6), 1157.
(49) Gadziński, P.; Froelich, A.; Wojtyłko, M.; Białek, A.; Krysztofiak, J.; Osmałek, T. Microneedle-based ocular drug delivery systems - recent advances and challenges. *Beilstein J. Nanotechnol* **2022**, *13*, 1167−1184.
(50) Razzaghi, M.; Seyfoori, A.; Pagan, E.; Askari, E.; Hassani Najafabadi, A.; Akbari, M. 3D Printed Hydrogel Microneedle Arrays for Interstitial Fluid Biomarker Extraction and Colorimetric Detection. *Polymers* **2023**, *15* (6), 1389.
(51) Tejavibulya, N.; Colburn, D. A. M.; Marcogliese, F. A.; Yang, K.-A.; Guo, V.; Chowdhury, S.; Stojanovic, M. N.; Sia, S. K. Hydrogel Microfilaments toward Intradermal Health Monitoring. *iScience* **2019**, *21*, 328−340.
(52) Johnson, A. R.; Procopio, A. T. Low cost additive manufacturing of microneedle masters. *3D Print Med.* **2019**, *5* (1), 2.
(53) Keirouz, A.; Mustafa, Y. L.; Turner, J. G.; Lay, E.; Jungwirth, U.; Marken, F.; Leese, H. S. Conductive Polymer-Coated 3D Printed Microneedles: Biocompatible Platforms for Minimally Invasive Biosensing Interfaces. *Small* **2023**, *19* (14), No. 2206301.
(54) Choo, S.; Jin, S.; Jung, J. Fabricating High-Resolution and High-Dimensional Microneedle Mold through the Resolution Improvement of Stereolithography 3D Printing. *Pharmaceutics* **2022**, *14* (4), 766.
(55) Pere, C. P. P.; Economidou, S. N.; Lall, G.; Ziraud, C.; Boateng, J. S.; Alexander, B. D.; Lamprou, D. A.; Douroumis, D. 3D printed microneedles for insulin skin delivery. *Int. J. Pharm.* **2018**, *544* (2), 425−432.
(56) Balmert, S. C.; Carey, C. D.; Falo, G. D.; Sethi, S. K.; Erdos, G.; Korkmaz, E.; Falo, L. D. Dissolving undercut microneedle arrays for multicomponent cutaneous vaccination. *J. Controlled Release* **2020**, *317*, 336−346.
(57) Economidou, S. N.; Pissinato Pere, C. P.; Okereke, M.; Douroumis, D. Optimisation of Design and Manufacturing Parameters of 3D Printed Solid Microneedles for Improved Strength, Sharpness, and Drug Delivery. *Micromachines* **2021**, *12* (2), 117.
(58) Tabriz, A. G.; Viegas, B.; Okereke, M.; Uddin, M. J.; Lopez, E. A.; Zand, N.; Ranatunga, M.; Getti, G.; Douroumis, D. Evaluation of 3D Printability and Biocompatibility of Microfluidic Resin for Fabrication of Solid Microneedles. *Micromachines* **2022**, *13* (9), 1368.
(59) Keirouz, A.; Mustafa, Y. L.; Turner, J. G.; Lay, E.; Jungwirth, U.; Marken, F.; Leese, H. S. Conductive Polymer-Coated 3D Printed Microneedles: Biocompatible Platforms for Minimally Invasive Biosensing Interfaces. *Small* **2023**, *19* (14), No. e2206301.
(60) Yadav, V.; Sharma, P. K.; Murty, U. S.; Mohan, N. H.; Thomas, R.; Dwivedy, S. K.; Banerjee, S. 3D printed hollow microneedles array using stereolithography for efficient transdermal delivery of rifampicin. *Int. J. Pharm.* **2021**, *605*, No. 120815.
(61) Yeung, C.; Chen, S.; King, B.; Lin, H.; King, K.; Akhtar, F.; Diaz, G.; Wang, B.; Zhu, J.; Sun, W. A 3D-printed microfluidic-enabled hollow microneedle architecture for transdermal drug delivery. *Biomicrofluidics* **2019**, *13* (6), 064125.

https://doi.org/10.1021/acsbiomaterials.4c00905
ACS Biomater. Sci. Eng. XXXX, XXX, XXX−XXX

(62) Chen, Y.; Chen, B. Z.; Wang, Q. L.; Jin, X.; Guo, X. D. Fabrication of coated polymer microneedles for transdermal drug delivery. *J. Controlled Release* **2017**, *265*, 14−21.
(63) Gill, H. S.; Prausnitz, M. R. Coated microneedles for transdermal delivery. *Journal of controlled release* **2007**, *117* (2), 227−237.
(64) Kim, S.-J.; Shin, J.-H.; Noh, J.-Y.; Song, C.-S.; Kim, Y.-C. Development of the novel coating formulations for skin vaccination using stainless steel microneedle. *Drug Delivery and Translational Research* **2016**, *6* (5), 486−497.
(65) Ma, Y.; Gill, H. S. Coating Solid Dispersions on Microneedles via a Molten Dip-Coating Method: Development and In Vitro Evaluation for Transdermal Delivery of a Water-Insoluble Drug. *Journal of pharmaceutical sciences* **2014**, *103* (11), 3621−3630.
(66) Liang, L.; Chen, Y.; Zhang, B. L.; Zhang, X. P.; Liu, J. L.; Shen, C. B.; Cui, Y.; Guo, X. D. Optimization of dip-coating methods for the fabrication of coated microneedles for drug delivery. *Journal of Drug Delivery Science and Technology* **2020**, *55*, No. 101464.
(67) Liang, L.; Zhao, Z. Q.; Chen, Y.; Ren, G. Y.; Li, J. Y.; Guo, X. D. Some attempts to increase the amount of drug coated onto the microneedles. *Journal of Drug Delivery Science and Technology* **2022**, *67*, No. 102986.
(68) Bera, B.; Backus, E. H. G.; Carrier, O.; Bonn, M.; Shahidzadeh, N.; Bonn, D. Antisurfactant (Autophobic) Behavior of Superspreader Surfactant Solutions. *Langmuir* **2021**, *37* (20), 6243−6247.
(69) Caton, P. W.; Kieswich, J.; Yaqoob, M. M.; Holness, M. J.; Sugden, M. C. Nicotinamide mononucleotide protects against pro-inflammatory cytokine-mediated impairment of mouse islet function. *Diabetologia* **2011**, *54* (12), 3083−3092.
(70) Ramsey, K. M.; Mills, K. F.; Satoh, A.; Imai, S.-i. Age-associated loss of Sirt1-mediated enhancement of glucose-stimulated insulin secretion in beta cell-specific Sirt1-overexpressing (BESTO) mice. *Aging Cell* **2008**, *7* (1), 78−88.
(71) Revollo, J. R.; Körner, A.; Mills, K. F.; Satoh, A.; Wang, T.; Garten, A.; Dasgupta, B.; Sasaki, Y.; Wolberger, C.; Townsend, R. R.; et al. Nampt/PBEF/Visfatin Regulates Insulin Secretion in β Cells as a Systemic NAD Biosynthetic Enzyme. *Cell Metabolism* **2007**, *6* (5), 363−375.
(72) Long, A. N.; Owens, K.; Schlappal, A. E.; Kristian, T.; Fishman, P. S.; Schuh, R. A. Effect of nicotinamide mononucleotide on brain mitochondrial respiratory deficits in an Alzheimer's disease-relevant murine model. *BMC Neurology* **2015**, *15* (1), 19.
(73) Klimova, N.; Long, A.; Kristian, T. Nicotinamide mononucleotide alters mitochondrial dynamics by SIRT3-dependent mechanism in male mice. *J. Neurosci Res.* **2019**, *97* (8), 975−990.
(74) Ji, J.; Damschroder, D.; Bessert, D.; Lazcano, P.; Wessells, R.; Reynolds, C. A.; Greenberg, M. L. NAD supplementation improves mitochondrial performance of cardiolipin mutants. *Biochim Biophys Acta Mol. Cell Biol. Lipids* **2022**, *1867* (4), No. 159094.
(75) Blake, T. D.; Ruschak, K. J. Wetting: static and dynamic contact lines. In *Liquid Film Coating: Scientific principles and their technological implications*; Springer, 1997; pp 63−97.
(76) Kontogiorgos, V.; Prakash, S. Adsorption kinetics and dilatational rheology of plant protein concentrates at the air- and oil-water interfaces. *Food Hydrocolloids* **2023**, *138*, No. 108486.
(77) Ghanbariamin, D.; Samandari, M.; Ghelich, P.; Shahbazmohamadi, S.; Schmidt, T. A.; Chen, Y.; Tamayol, A. Cleanroom-Free Fabrication of Microneedles for Multimodal Drug Delivery. *Small* **2023**, *19* (29), No. 2207131.
(78) Jing, Q.; Ruan, H.; Li, J.; Wang, Z.; Pei, L.; Hu, H.; He, Z.; Wu, T.; Ruan, S.; Guo, T.; et al. Keratinocyte membrane-mediated nanodelivery system with dissolving microneedles for targeted therapy of skin diseases. *Biomaterials* **2021**, *278*, No. 121142.
(79) Seo, M. D.; Kang, T. J.; Lee, C. H.; Lee, A. Y.; Noh, M. HaCaT Keratinocytes and Primary Epidermal Keratinocytes Have Different Transcriptional Profiles of Cornified Envelope-Associated Genes to T Helper Cell Cytokines. *Biomol Ther (Seoul)* **2012**, *20* (2), 171−176.
(80) Farias, C.; Lyman, R.; Hemingway, C.; Chau, H.; Mahacek, A.; Bouzos, E.; Mobed-Miremadi, M. Three-Dimensional (3D) Printed Microneedles for Microencapsulated Cell Extrusion. *Bioengineering* **2018**, *5* (3), 59.
(81) Moussi, K.; Bukhamsin, A.; Hidalgo, T.; Kosel, J. Biocompatible 3D Printed Microneedles for Transdermal, Intradermal, and Percutaneous Applications. *Adv. Eng. Mater.* **2020**, *22* (2), No. 1901358.
(82) Schuh, J. C. L.; Funk, K. A. Compilation of International Standards and Regulatory Guidance Documents for Evaluation of Biomaterials, Medical Devices, and 3-D Printed and Regenerative Medicine Products. *Toxicologic Pathology* **2019**, *47* (3), 344−357.
(83) Rauf, M. A.; Graham, J. P.; Bukallah, S. B.; Al-Saedi, M. A. S. Solvatochromic behavior on the absorption and fluorescence spectra of Rose Bengal dye in various solvents. *Spectrochimica Acta Part A: Molecular and Biomolecular Spectroscopy* **2009**, *72* (1), 133−137.
(84) Larrañeta, E.; Moore, J.; Vicente-Pérez, E. M.; González-Vázquez, P.; Lutton, R.; Woolfson, A. D.; Donnelly, R. F. A proposed model membrane and test method for microneedle insertion studies. *Int. J. Pharm.* **2014**, *472* (1−2), 65−73.
(85) Marinescu, G. C.; Popescu, R.-G.; Dinischiotu, A. Size Exclusion Chromatography Method for Purification of Nicotinamide Mononucleotide (NMN) from Bacterial Cells. *Sci. Rep.* **2018**, *8* (1), 4433−4433.
(86) Nastiti, C. M. R. R.; Ponto, T.; Mohammed, Y.; Roberts, M. S.; Benson, H. A. E. Novel Nanocarriers for Targeted Topical Skin Delivery of the Antioxidant Resveratrol. *Pharmaceutics* **2020**, *12* (2), 108.
(87) Telaprolu, K. C.; Grice, J. E.; Mohammed, Y. H.; Roberts, M. S. Human Skin Drug Metabolism: Relationships between Methyl Salicylate Metabolism and Esterase Activities in IVPT Skin Membranes. *Metabolites* **2023**, *13* (8), 934.
(88) Nastiti, C. M. R. R.; Mohammed, Y.; Telaprolu, K. C.; Liang, X.; Grice, J. E.; Roberts, M. S.; Benson, H. A. E. Evaluation of Quantum Dot Skin Penetration in Porcine Skin: Effect of Age and Anatomical Site of Topical Application. *Skin Pharmacology and Physiology* **2019**, *32* (4), 182−191.
(89) Mohammed, Y. H.; Haridass, I. N.; Grice, J. E.; Benson, H. A. E.; Roberts, M. S. Bathing Does Not Facilitate Human Skin Penetration or Adverse Cellular Effects of Nanoparticulate Zinc Oxide Sunscreens after Topical Application. *J. Invest Dermatol* **2020**, *140* (8), 1656−1659.
(90) Mohammed, Y.; Barkauskas, D.; Holmes, A.; Grice, J.; Roberts, M. Noninvasive in vivo human multiphoton microscopy: a key method in proving nanoparticulate zinc oxide sunscreen safety. *Journal of Biomedical Optics* **2020**, *25* (1), No. 014509.
(91) Leite-Silva, V. R.; Sanchez, W. Y.; Studier, H.; Liu, D. C.; Mohammed, Y. H.; Holmes, A. M.; Ryan, E. M.; Haridass, I. N.; Chandrasekaran, N. C.; Becker, W.; et al. Human skin penetration and local effects of topical nano zinc oxide after occlusion and barrier impairment. *Eur. J. Pharm. Biopharm.* **2016**, *104*, 140−147.
(92) Cao, R.; Wallrabe, H.; Periasamy, A. Multiphoton FLIM imaging of NAD(P)H and FAD with one excitation wavelength. *J. Biomed Opt* **2020**, *25* (1), 1−16.
(93) Prausnitz, M. R. Engineering microneedle patches for vaccination and drug delivery to skin. *Annu. Rev. Chem. Biomol. Eng.* **2017**, *8*, 177−200.
(94) Loh, J. M.; Lim, Y. J. L.; Tay, J. T.; Cheng, H. M.; Tey, H. L.; Liang, K. Design and fabrication of customizable microneedles enabled by 3D printing for biomedical applications. *Bioactive Materials* **2024**, *32*, 222−241.
(95) Palmara, G.; Frascella, F.; Roppolo, I.; Chiappone, A.; Chiadò, A. Functional 3D printing: Approaches and bioapplications. *Biosens. Bioelectron.* **2021**, *175*, No. 112849.
(96) Holmes, R.; Yang, X. B.; Dunne, A.; Florea, L.; Wood, D.; Tronci, G. Thiol-Ene Photo-Click Collagen-PEG Hydrogels: Impact of Water-Soluble Photoinitiators on Cell Viability, Gelation Kinetics and Rheological Properties. *Polymers (Basel)* **2017**, *9* (6), 226.
(97) Venzac, B.; Deng, S.; Mahmoud, Z.; Lenferink, A.; Costa, A.; Bray, F.; Otto, C.; Rolando, C.; Le Gac, S. PDMS Curing Inhibition

https://doi.org/10.1021/acsbiomaterials.4c00905
ACS Biomater. Sci. Eng. XXXX, XXX, XXX−XXX

on 3D-Printed Molds: Why? Also, How to Avoid It? *Anal. Chem.* **2021**, *93* (19), 7180−7187.
(98) Zhang, Y.; Brown, K.; Siebenaler, K.; Determan, A.; Dohmeier, D.; Hansen, K. Development of lidocaine-coated microneedle product for rapid, safe, and prolonged local analgesic action. *Pharm. Res.* **2012**, *29* (1), 170−177.
(99) Ita, K. Transdermal Delivery of Drugs with Microneedles-Potential and Challenges. *Pharmaceutics* **2015**, *7* (3), 90−105.
(100) He, X.; Sun, J.; Zhuang, J.; Xu, H.; Liu, Y.; Wu, D. Microneedle System for Transdermal Drug and Vaccine Delivery: Devices, Safety, and Prospects. *Dose-response* **2019**, *17* (4), 155932581987858.
(101) Mertsching, H.; Weimer, M.; Kersen, S.; Brunner, H. Human skin equivalent as an alternative to animal testing. *GMS Krankenhhyg Interdiszip* **2008**, *3* (1), Doc11.
(102) Chellathurai, M. S.; Ling, V. W. T.; Palanirajan, V. K. Fabrication and Evaluation of Transdermal Microneedles for a Recombinant Human Keratinocyte Growth Factor. *Turk J. Pharm. Sci.* **2021**, *18* (1), 96−103.
(103) Forouz, F.; Mohammed, Y.; Shobeiri Nejad, H. S. A.; Roberts, M. S.; Grice, J. E. In vitro screening of topical formulation excipients for epithelial toxicity in cancerous and non-cancerous cell lines. *Excli j* **2023**, *22*, 1173−1199.
(104) Elsabahy, M.; Wooley, K. L. Cytokines as biomarkers of nanoparticle immunotoxicity. *Chem. Soc. Rev.* **2013**, *42* (12), 5552−5576.
(105) Economidou, S. N.; Pere, C. P. P.; Reid, A.; Uddin, M. J.; Windmill, J. F. C.; Lamprou, D. A.; Douroumis, D. 3D printed microneedle patches using stereolithography (SLA) for intradermal insulin delivery. *Materials Science and Engineering: C* **2019**, *102*, 743−755.
(106) Kim, M.; Park, S.; Choi, S.-O. Dual-nozzle spray deposition process for improving the stability of proteins in polymer microneedles. *RSC Adv.* **2017**, *7*, 55350−55359.
(107) Donnelly, R. F.; Majithiya, R.; Singh, T. R. R.; Morrow, D. I. J.; Garland, M. J.; Demir, Y. K.; Migalska, K.; Ryan, E.; Gillen, D.; Scott, C. J.; et al. Design, Optimization and Characterisation of Polymeric Microneedle Arrays Prepared by a Novel Laser-Based Micromoulding Technique. *Pharm. Res.* **2011**, *28* (1), 41−57.
(108) DeMuth, P. C.; Li, A. V.; Abbink, P.; Liu, J.; Li, H.; Stanley, K. A.; Smith, K. M.; Lavine, C. L.; Seaman, M. S.; Kramer, J. A.; et al. Vaccine delivery with microneedle skin patches in nonhuman primates. *Nat. Biotechnol.* **2013**, *31* (12), 1082−1085.
(109) Nadeeshani, H.; Li, J.; Ying, T.; Zhang, B.; Lu, J. Nicotinamide mononucleotide (NMN) as an anti-aging health product−promises and safety concerns. *Journal of advanced research* **2022**, *37*, 267−278.
(110) Yi, L.; Maier, A. B.; Tao, R.; Lin, Z.; Vaidya, A.; Pendse, S.; Thasma, S.; Andhalkar, N.; Avhad, G.; Kumbhar, V. The efficacy and safety of β-nicotinamide mononucleotide (NMN) supplementation in healthy middle-aged adults: a randomized, multicenter, double-blind, placebo-controlled, parallel-group, dose-dependent clinical trial. *GeroScience* **2023**, *45* (1), 29−43.
(111) Tsubota, K. The first human clinical study for NMN has started in Japan. *npj Aging and Mechanisms of Disease* **2016**, *2* (1), No. 16021.
(112) Youngson, N. A.; Uddin, G. M.; Das, A.; Martinez, C.; Connaughton, H. S.; Whiting, S.; Yu, J.; Sinclair, D. A.; Aitken, R. J.; Morris, M. J. Impacts of obesity, maternal obesity and nicotinamide mononucleotide supplementation on sperm quality in mice. *Reproduction* **2019**, *158* (2), 171.
(113) Pencina, K. M.; Lavu, S.; dos Santos, M.; Beleva, Y. M.; Cheng, M.; Livingston, D.; Bhasin, S. MIB-626, an Oral Formulation of a Microcrystalline Unique Polymorph of β-Nicotinamide Mononucleotide, Increases Circulating Nicotinamide Adenine Dinucleotide and its Metabolome in Middle-Aged and Older Adults. *Journals of Gerontology: Series A* **2023**, *78* (1), 90−96.
(114) Toaquiza Tubon, J. D.; Moreno-Flores, O.; Sree, V.; Tepole, A. B. Anisotropic damage model for collagenous tissues and its application to model fracture and needle insertion mechanics. *Biomechanics and Modeling in Mechanobiology* **2022**, *21*, 1−16.
(115) Benítez, J. M.; Montáns, F. J. The mechanical behavior of skin: Structures and models for the finite element analysis. *Computers & Structures* **2017**, *190*, 75−107.
(116) Haridass, I. N.; Wei, J. C. J.; Mohammed, Y. H.; Crichton, M. L.; Anderson, C. D.; Henricson, J.; Sanchez, W. Y.; Meliga, S. C.; Grice, J. E.; Benson, H. A. E.; et al. Cellular metabolism and pore lifetime of human skin following microprojection array mediation. *J. Controlled Release* **2019**, *306*, 59−68.
(117) Chen, J.; Qiu, Y.; Zhang, S.; Yang, G.; Gao, Y. Controllable coating of microneedles for transdermal drug delivery. *Drug Dev. Ind. Pharm.* **2015**, *41* (3), 415−422.
(118) Costa, P.; Sousa Lobo, J. M. Modeling and comparison of dissolution profiles. *European Journal of Pharmaceutical Sciences* **2001**, *13* (2), 123−133.
(119) Zhao, Y.; Li, W.; Shi, Z.; Drennen, J. K.; Anderson, C. A. Prediction of Dissolution Profiles From Process Parameters, Formulation, and Spectroscopic Measurements. *J. Pharm. Sci.* **2019**, *108* (6), 2119−2127.

https://doi.org/10.1021/acsbiomaterials.4c00905
ACS Biomater. Sci. Eng. XXXX, XXX, XXX−XXX